Research Square

Preprints are preliminary reports that have not undergone peer review.
They should not be considered conclusive, used to inform clinical practice,
or referenced by the media as validated information.

The necrotic niche is a lipid reservoir coupling tumour fitness to metabolic vulnerability

Mattias Belting

mattias.belting@med.lu.se

Lund University, Department of Clinical Sciences, Division of Oncology; Skåne University Hospital, Department of Hematology, Oncology and Radiophysics https://orcid.org/0000-0003-1585-5434

Hugo Talbot

Lund University, Department of Clinical Sciences, Division of Oncology https://orcid.org/0000-0001-9774-8573

Myriam Cerezo-Magaña

Lund University, Department of Clinical Sciences, Division of Oncology https://orcid.org/0000-0001-9752-8917

Euisuk Han

Lund University, Department of Clinical Sciences, Division of Oncology

Darko Tamindzic

Lund University, Department of Clinical Sciences, Division of Oncology

Emma Gustafsson

Lund University https://orcid.org/0009-0007-7005-912X

Axel Boukredine

Lund University https://orcid.org/0009-0006-3714-6769

Federica Trippitelli

Lund University https://orcid.org/0009-0006-8862-3377

Anna Bång-Rudenstam

Lund University https://orcid.org/0000-0003-2706-9502

Stevanus Jonathan

Lund University, Department of Clinical Sciences, Division of Neurosurgery https://orcid.org/0009-0000-4349-5371

Sarah Beyer

Lund University, Department of Clinical Sciences, Division of Oncology

Charlotte Edvardsson

Lund University, Department of Clinical Sciences, Division of Neurosurgery; Skåne University Hospital, Department of Neurosurgery

Maria C Johansson

Lund University https://orcid.org/0000-0003-0075-3187

Sebastián Barrientos Baeza
Lund University, Department of Laboratory Medicine, Division of Translational Cancer Research
Ramin Massoumi
Lund University, Department of Laboratory Medicine, Division of Translational Cancer Research
Anna Darabi
Lund University
Johan Bengzon
Skane University Hospital
Valeria Governa
Lund University, Department of Clinical Sciences, Section of Oncology https://orcid.org/0000-0001-9999-0590

Biological Sciences - Article

Keywords:

Posted Date: September 9th, 2026

DOI: https://doi.org/10.21203/rs.3.rs-10801793/v1

License: This work is licensed under a Creative Commons Attribution 4.0 International License.
Read Full License

Additional Declarations: There is **NO** Competing Interest.

The necrotic niche is a lipid reservoir coupling tumour fitness to metabolic vulnerability

Hugo Talbot[1,*], Myriam Cerezo-Magaña[1], Euisuk Han[1], Darko Tamindzic[1], Emma Gustafsson[1], Axel Boukredine[1], Federica Trippitelli[1], Anna Bång-Rudenstam[1], Stevanus Jonathan[3], Sarah Beyer[1], Charlotte Edvardsson[2,3], Maria C Johansson[1], Sebastián Barrientos Baeza[4], Ramin Massoumi[4], Anna Darabi[2], Johan Bengzon[2,3], Valeria Governa[1], & Mattias Belting[1,5,*]

[1]Department of Clinical Sciences, Division of Oncology, Lund University, Lund, Sweden.

[2]Department of Clinical Sciences, Division of Neurosurgery, Lund University, Lund, Sweden.

[3]Department of Neurosurgery, Skåne University Hospital, Lund, Sweden.

[4]Department of Laboratory Medicine, Division of Translational Cancer Research, Lund University, Lund, Sweden.

[5]Department of Hematology, Oncology and Radiophysics, Skåne University Hospital, Lund, Sweden.

[*]Lead contacts: Mattias Belting and Hugo Tabot, Department of Clinical Sciences, Division of Oncology, Lund University, Barngatan 4, SE-221 85, Lund, Sweden; Tel: +46-46-178549; E-mail: mattias.belting@med.lu.se; hugo.talbot@med.lu.se

Abstract

Necrosis is a defining feature of aggressive tumours but is generally regarded as a consequence of metabolic failure, despite increasing evidence that necrotic regions actively remodel the tumour microenvironment[1–3]. Cancer cells adapt to nutrient limitation through scavenging pathways that provide alternative metabolic resources[4,5], yet whether they directly exploit necrotic biomass and how this influences tumour adaptation remain poorly understood. Here, using human glioblastoma (GBM) as a model, we identify the necrotic niche as a lipid reservoir that simultaneously promotes tumour fitness and creates metabolic vulnerability. GBM cells actively scavenge necrotic debris through a dynamin- and membrane raft-dependent endocytic pathway, transferring necrotic lipids into lipid droplets (LDs) and enhancing bioenergetic capacity, proliferation, radioresistance and tumorigenicity. Extending the emerging concept of non-professional phagocytosis in tissue homeostasis[6], debris-conditioned tumour cells additionally promote myeloid recruitment and formation of lipid-laden foam cell-like macrophages. Mechanistically, LD biogenesis buffers necrosis-derived lipid stress and is required for the fitness benefits of debris scavenging. Disrupting LD formation, however, does not induce cell death but activates compensatory anti-ferroptotic programmes involving SLC7A11 and CPT1A that preserve tumour cell viability. Combined targeting of LD buffering and these defences triggers lipid peroxidation and ferroptotic cell death, while co-inhibition of LD biogenesis and SLC7A11 prolongs survival in an orthotopic tumour model. Our findings establish necrotic biomass as a metabolic resource whose exploitation promotes tumour fitness while creating targetable dependencies on lipid buffering and ferroptosis defence.

Main

Tumour growth imposes bioenergetic demands that exceed the capacity of an abnormal tumour vasculature to supply oxygen and nutrients, ultimately resulting in extensive necrosis. Although necrosis has traditionally been viewed as a passive consequence of metabolic collapse, increasing evidence suggests that it contributes to tumour progression and remodelling of the tumour microenvironment (TME)[1,2,7]. In glioblastoma (GBM), one of the most lethal human malignancies, profound necrosis is a defining histopathological feature associated with tumour aggressiveness and poor patient survival[1,2,7]. However, whether necrotic regions function as metabolically active niches that drive tumour adaptation and create therapeutically exploitable metabolic vulnerabilities remains unknown.

The perinecrotic niche represents a state of profound metabolic constraint[2,3,7,8]. To survive under these conditions, cancer cells engage macropinocytosis and other endocytic pathways to acquire nutrients that sustain anabolic metabolism, therapeutic resistance and tumour growth[4,5,9,10]. Necrotic debris, however, represents a distinct source of complex cellular biomass, including membranes and oxidizable lipids that must be accommodated without inducing lipotoxicity and ferroptotic cell death[11–14]. Lipid droplets (LDs) are dynamic organelles that sequester excess fatty acids as neutral lipids, thereby shielding cells from oxidative damage[15,16]. Consequently, diacylglycerol O-acyltransferase 1 (DGAT1), which catalyses the final step of triglyceride synthesis and LD biogenesis, has emerged as a potential therapeutic target in several cancers, including GBM[11,15,17]. However, whether LDs provide the metabolic buffering required to exploit necrotic biomass, and whether disruption of this buffering creates therapeutically targetable dependencies, remains unknown.

Here, we identify necrotic debris scavenging as a metabolic adaptation pathway in GBM that couples necrotic lipid acquisition to coordinated lipid buffering and anti-ferroptotic defence. We show that tumour cells themselves actively internalize necrotic debris through a dynamin- and membrane raft- dependent endocytic mechanism, resulting in LD accumulation and increased tumour fitness. LD formation buffers necrosis-derived lipid stress, while its disruption activates compensatory anti-ferroptotic pathways that preserve cell viability. Combined disruption of lipid buffering and anti-ferroptotic defence induces ferroptotic cell death and exposes a therapeutic vulnerability within the perinecrotic niche.

GBM cells scavenge and buffer lipids from necrotic debris

Human GBM tissue sections displayed prominent LD accumulation in perinecrotic regions, and analysis of separately resected necrotic and viable tumour tissue confirmed LD enrichment in the necrotic fraction (Extended Data Fig. 1a,b). This spatial association was recapitulated in primary patient-derived GBM spheroids and in orthotopic SB28 tumours, where LDs similarly localized to necrotic areas (Extended Data Fig. 1c,d). These observations raised the possibility that necrotic material itself contributes to LD accumulation within the perinecrotic niche. To test this idea, we generated necrotic glioma cell debris by freeze-thawing (NecD), high-dose irradiation (NecD-IR) or prolonged starvation (NecD-Starv) and, additionally, freshly resected patient-derived necrotic material (NecD-P) (Extended Data Fig. 1e). Both patient-derived NecD-P and NecD induced LD accumulation, albeit to varying extents across multiple GBM cultures (Fig. 1a-d). In a direct comparison, NecD and NecD-P elicited comparable LD induction (Fig. 1e). Primary cell-derived NecD-IR and NecD-Starv similarly promoted LD accumulation in recipient GBM cells (Extended Data Fig. 1f,g), suggesting that lipid buffering represents a common response to diverse forms of

necrosis. LD induction was concentration- and time-dependent (Extended Data Fig. 1h,i) and originated predominantly from the cellular debris fraction rather than the soluble compartment (Extended Data Fig. 1j,k). Notably, LD formation was not impaired by fatty acid synthase (FASN) inhibition (Extended Data Fig. 1l), supporting a predominant contribution of scavenged lipids rather than *de novo* lipogenesis.

Whereas debris scavenging is an established function of macrophages, the mechanisms by which tumour cells scavenge necrotic debris remain poorly defined[5]. To trace the fate of distinct NecD constituents, we metabolically labelled donor cells and monitored transfer of NecD-associated proteins, nucleic acids and lipids into recipient GBM cells (Fig. 1f and Extended Data Fig. 2a). All three macromolecular classes were efficiently internalized (Fig. 1g and Extended Data Fig. 2b,c) and localized to Early Endosome Antigen 1 (EEA1)-positive endocytic compartments of recipient cells (Extended Data Fig. 2d-f). Lipid tracing using BODIPY-DA (dodecanoic acid)-labelling further confirmed transfer of NecD-derived lipids into recipient cells (Fig. 1g and Extended Data Fig. 2b-d and f) and revealed dose-dependent uptake of NecD (Fig. 1h and Extended Data Fig. 2g), patient-derived NecD-P (Extended Data Fig. 2h) and NecD-IR (Extended Data Fig. 2i). Both human and mouse GBM cells displayed time-dependent, saturable uptake (Fig. 1i and Extended Data Fig. 2j) that was inhibited by low temperature, competition with excess unlabelled NecD, and proteolytic or heat-mediated disruption of necrotic material (Extended Data Fig. 2k-n), whereas transfer of BODIPY-DA from the soluble NecD cell fraction was negligible (Extended Data Fig. 2o). Together, these data indicate an active, regulated scavenging process dependent on NecD-associated protein determinants.

These findings prompted us to investigate the endocytic pathway underlying NecD uptake. Although macropinocytosis has emerged as an important scavenging mechanism in nutrient-

limited tumours[4,5,9], pharmacological inhibition of macropinocytosis had no effect on NecD uptake in GBM cells (Extended Data Fig. 2p). By contrast, NecD internalization was efficiently suppressed by β-methyl-cyclodextrin (MCD) and Dynasore (Fig. 1j,k and Extended Data Fig. 2q), supporting involvement of cholesterol-rich membrane domains and dynamin-dependent endocytosis[18]. NecD uptake by primary GBM cultures (Fig. 1l and Extended Data Fig. 2r) correlated with cholera toxin B (CtxB) internalization (Extended Data Fig. 2s), consistent with involvement of a raft-associated uptake pathway[19]. Importantly, NecD uptake activity was associated with the extent of LD accumulation across GBM cultures (cf. Fig. 1d and l), and inhibition of endocytosis effectively suppressed NecD-dependent LD formation (Fig. 1m,n and Extended Data Fig. 2t). Direct lipid-transfer assays[19] confirmed incorporation of NecD-derived BODIPY-DA lipid tracer into recipient-cell LDs, as demonstrated by co-localization with the neutral lipid marker LipidTOX (Fig. 1o and Extended Data Fig. 2u). Together, these findings define necrotic debris scavenging as a raft-associated, dynamin-dependent endocytic process that channels necrotic lipids into LDs.

Necrotic debris scavenging promotes GBM fitness

To determine whether NecD scavenging induces a broader adaptive program, we performed transcriptomic analysis of the classical subtype primary GBM culture U3017MG[20]. NecD induced mesenchymal, inflammatory and pro-angiogenic programs, together with pathways associated with lipid storage and oxidative stress responses (Fig. 2a and Extended Data Tables 1 and 2). From the top-contributing genes across these programs, we derived a NecD-associated transcriptional signature (Fig. 2b and Extended Data Table 1). This signature was enriched in LD-rich regions compared with matched LD-negative regions isolated by laser-capture microdissection from fresh-

frozen patient tumours (Fig. 2b,c). In The Cancer Genome Atlas (TCGA) GBM and low-grade glioma (LGG) cohorts, the NecD signature was enriched in GBM versus LGG (Extended Data Fig. 3a) and in recurrent versus primary GBM (Extended Data Fig. 3b). Furthermore, the signature was strongly associated with the mesenchymal GBM subtype (Fig. 2d), was preferentially enriched in pseudopalisading/perinecrotic regions (Fig. 2e), and its high expression correlated with reduced overall survival (Fig. 2f).

The transcriptional reprogramming induced by NecD scavenging raised the possibility that this adaptive state confers functional advantages to GBM cells. NecD dose-dependently enhanced DNA synthesis, mitochondrial function and bioenergetic capacity in U87MG cells, leading to increased tumour cell growth *in vitro* (Fig. 2g-j). NecD pre-loading additionally accelerated spheroid expansion (Extended Data Fig. 3c). Similar growth-promoting effects were observed across a panel of primary GBM cultures following NecD scavenging (Fig. 2k), and patient-derived NecD-P (Fig. 2l) as well as NecD-IR (Extended Data Fig. 3d,e) elicited comparable responses. Moreover, radiation-sensitive primary GBM cultures acquired dose-dependent radioresistance following NecD scavenging (Fig. 2m and Extended Data Fig. 3f), while radiation-insensitive cultures maintained the proliferative advantage associated with NecD exposure (Extended Data Fig. 3g). Transcriptomic analysis of the most radiosensitive primary GBM culture (U3017MG) revealed that NecD scavenging partially reversed irradiation-induced transcriptional programs associated with DNA damage responses while restoring pathways linked to cell-cycle progression and mitosis (Extended Data Fig. 3h and Extended Data Tables 1 and 3).

To assess whether NecD scavenging promotes tumour fitness *in vivo*, we orthotopically injected NecD-conditioned U87MG cells into NSG mice. Whereas control cells showed minimal tumour growth after 21 days, NecD-conditioned cells formed large tumours (Extended Data Fig. 3i).

Because this xenograft model lacked prominent necrotic and LD-rich regions[21], we next evaluated NecD effects in the syngeneic SB28 model, which recapitulated both features within an intact immune microenvironment (Extended Data Fig. 1d). Orthotopic implantation of SB28 cells preconditioned with autologous NecD (Fig. 2n) significantly reduced overall survival compared with control cells (Fig. 2o). Collectively, these findings establish necrotic debris scavenging as an adaptive program that promotes GBM fitness across experimental systems and disease-relevant contexts.

Necrotic debris scavenging promotes inflammatory signalling and myeloid lipid accumulation

Transcriptomic analyses of NecD-conditioned GBM cells revealed robust induction of cytokines and chemokines implicated in myeloid cell recruitment and activation, including *IL1B*, *IL36B, IL6*, *CXCL8* and *CSF3* (Extended Data Fig. 4a). Upregulation of *IL1B* following NecD scavenging was confirmed across multiple primary GBM cultures (Extended Data Fig. 4b). To determine whether this inflammatory program influences the myeloid compartment, we exposed primary human myeloid cells to conditioned medium (CM) derived from NecD-conditioned GBM cells (Extended Data Fig. 4c). CM from three independent NecD-conditioned patient-derived GBM cultures promoted primary human monocyte recruitment compared with CM from control GBM cells (Extended Data Fig. 4d). Moreover, hypoxic M0 macrophages exposed to CM from NecD-loaded GBM cells acquired a lipid-laden phenotype characterized by LD accumulation (Extended Data Fig. 4e) and increased expression of PD-L1 (Extended Data Fig. 4f), consistent with the tumour-associated foam cell (TAF) phenotype previously identified in perinecrotic regions of human GBM[21]. Extending these observations to the *in vivo* setting, TAF-like cells were markedly enriched

within perinecrotic regions of SB28 tumours compared with viable tumour areas (Extended Data Fig. 4g). Together, these findings suggest that necrotic debris scavenging couples tumour-intrinsic metabolic adaptation to inflammatory crosstalk with myeloid cells, promoting their recruitment and acquisition of a TAF-like phenotype.

LD biogenesis underpins NecD-induced tumour fitness but is dispensable for survival

We next investigated whether the tumour-promoting effects of NecD scavenging depend on LD biogenesis and utilization. Pharmacological inhibition of DGAT1 using A922500 (DGAT1i)[11,15,17,21] efficiently disrupted LD accumulation in NecD- (Fig. 3a,b), NecD-P- (Extended Data Fig. 5a), and NecD-IR-conditioned (Extended Data Fig. 5b) GBM cells. DGAT1 inhibition did not affect NecD uptake (Extended Data Fig. 5c), demonstrating that impaired LD formation is not a consequence of reduced debris scavenging. Importantly, DGAT1 inhibition abolished the growth-promoting effects of NecD in U87MG cells (Fig. 3c) and primary GBM cultures (Fig. 3d and Extended Data Fig. 5d). Similar results were obtained with Triacsin C, an inhibitor of long-chain acyl-CoA synthetase (ACSL)-dependent LD formation[22] (Fig. 3e,f), indicating that the observed effects were not specific to DGAT1 inhibition. Disruption of LD biogenesis impaired metabolic activity and mitochondrial integrity (Fig. 3g-i), and inhibition of LD lipolysis using Atglistatin[23] (Extended Data Fig. 5e) attenuated tumour cell growth (Extended Data Fig. 5f), supporting a role for NecD-induced LDs as metabolically accessible lipid reservoirs that sustain tumour cell fitness. Moreover, the radioprotective effects of NecD depended on LD functionality, as inhibition of either LD biogenesis (Fig. 3j, left) or lipolysis (Fig. 3j, right) partially restored radiation sensitivity.

We next examined primary GBM spheroids, which recapitulate key features of tumour architecture and spontaneously develop central necrosis accompanied by LD accumulation (Extended Data Fig. 1c). Analysis of spheroid sections and live spheroid imaging confirmed efficient suppression of core LD accumulation following DGAT1 inhibition (Fig. 3k and Extended Data Fig. 5g). Despite robust disruption of LD formation, DGAT1 inhibition attenuated spheroid expansion without inducing significant cytotoxicity (Fig. 3l,m). Thus, despite attenuating tumour growth, effective suppression of LD biogenesis was insufficient to induce cell death, suggesting that compensatory mechanisms maintain tumour cell survival under necrotic lipid overload.

Disruption of NecD-induced lipid buffering activates compensatory anti-ferroptotic programs

We next explored the adaptive mechanisms that maintain tumour cell survival under conditions of necrotic lipid overload. NecD scavenging induced expression of genes associated with reactive oxygen species (ROS) responses and ferroptosis suppression[12–14], whereas combined NecD loading and DGAT1 inhibition additionally enriched pathways linked to lipid oxidation and ferroptosis driver and suppressor programs (Fig. 4a,b and Extended Data Tables 1 and 4). Ferroptosis driver and suppressor pathways were also enriched in pseudopalisading/perinecrotic regions of patient tumours (Fig. 4c). Among established ferroptosis suppressors, solute carrier family 7 member 11 (SLC7A11), a cystine/glutamate antiporter[24,25], emerged as one of the most induced genes following combined NecD scavenging and DGAT1 inhibition, as demonstrated by transcriptomic and qRT-PCR analyses (Fig. 4b,d and Extended Data Fig. 6a,b). By contrast, other canonical ferroptosis suppressors, including glutathione peroxidase 4 (GPX4)[12,26,27], showed little or no induction (Fig. 4b), identifying SLC7A11 as a prominent candidate adaptive defence

mechanism engaged upon disruption of NecD-induced lipid buffering. In patient-derived GBM specimens, primary GBM spheroids and SB28 tumours, SLC7A11 expression localized predominantly to LD-rich, perinecrotic regions (Fig. 4e-h and Extended Data Fig. 6c), whereas LGG tumours displayed minimal SLC7A11 expression (Extended Data Fig. 6d). Supporting its association with adaptation to necrotic lipid stress, SLC7A11 expression was further enhanced upon DGAT1 inhibition in both human and SB28 GBM spheroids (Fig. 4i,j and Extended Data Fig. 6e).

To test whether SLC7A11 functionally compensates for impaired LD buffering, we quantified lipid peroxidation using the fluorescent lipid oxidation reporter C11-BODIPY581/591. Whereas inhibition of either DGAT1 or SLC7A11 alone had limited effects, combined treatment with DGAT1i and the SLC7A11 inhibitor erastin[28] markedly increased lipid peroxidation (Fig. 4k and Extended Data Fig. 6f). Combined inhibition was further associated with elevated levels of labile iron (Fig. 4l and Extended Data Fig. 6g), consistent with an iron-dependent pro-ferroptotic state[29]. The combinatorial induction of lipid peroxidation extended to multiple spheroid models following DGAT1i plus erastin treatment (Fig. 5a and Extended Data Fig. 7a). Carnitine palmitoyl transferase 1A (CPT1A), a regulator of mitochondrial fatty acid transport[30], was strongly induced by NecD lipid overload (Fig. 4b and Extended Data Fig. 7b) and its expression overlapped with LDs and SLC7A11 in perinecrotic regions (Extended Data Fig. 7c), raising the possibility that this pathway also contributes to adaptation to impaired lipid buffering. Supporting this notion, combined inhibition of DGAT1 and CPT1A using etomoxir similarly increased lipid peroxidation (Fig. 5b and Extended Data Fig. 7d). Both combinations also increased accumulation of malondialdehyde (MDA; Fig. 5c), a terminal product of lipid peroxidation, supporting SLC7A11

and CPT1A as adaptive defence pathways that limit oxidative lipid stress following disruption of NecD-induced lipid buffering.

We reasoned that these adaptive pathways might represent therapeutic dependencies imposed by necrotic debris scavenging. In primary GBM spheroids, combined targeting of DGAT1 and SLC7A11 or CPT1A increased cell death, as evidenced by TUNEL staining of spheroid sections (Fig. 5d) and live spheroid imaging (Fig. 5e,f). Whereas DGAT1i, erastin and etomoxir individually exhibited no discernible cytotoxic effects, the combination treatments resulted in spheroid shrinkage together with pronounced cytotoxicity (Fig. 5e,f). The cytotoxic effects of combination treatments were confirmed across multiple GBM cultures (Extended Data Fig. 7e,f). Further supporting involvement of the ferroptosis defence machinery, combined inhibition of DGAT1 and GPX4 using RSL3 phenocopied the cytotoxic effects of DGAT1i plus erastin or etomoxir (Extended Data Fig. 7g). Although GPX4 itself was not induced by NecD lipid overload (Fig. 4b), this finding links the observed vulnerability to disruption of the downstream glutathione-GPX4 antioxidant axis[12,26,31]. Indeed, both lipid peroxidation and cytotoxicity induced by DGAT1i plus erastin (Fig. 5g and Extended Data Fig. 7h) or DGAT1i plus etomoxir (Fig. 5h and Extended Data Fig. 7i) were effectively attenuated by the lipid-soluble antioxidant α-tocopherol. Together, these findings demonstrate that tumour cells rely on SLC7A11- and CPT1A-dependent adaptive programs when LD-mediated buffering is impaired, exposing conditional therapeutic dependencies created by necrotic debris scavenging and lipid stress.

Combined targeting of LD buffering and SLC7A11 exposes a therapeutic vulnerability in necrotic GBM

To assess whether the vulnerability created by combined LD disruption and SLC7A11 inhibition extends *in vivo*, we used the aggressive syngeneic SB28 model, which recapitulates NecD scavenging, LD accumulation and SLC7A11-rich perinecrotic regions (Extended Data Fig. 1d,h, Extended Data Fig. 2g, Extended Data Fig. 6c, and Fig. 4j). Combined inhibition of DGAT1 and either SLC7A11 (Fig. 6a) or GPX4 (Extended Data Fig. 8a) induced pronounced SB28 cell death, accompanied by increased lipid peroxidation as evidenced by MDA staining (Fig. 6b and Extended Data Fig. 8b). Live-cell imaging of SB28-GFP spheroids further revealed marked loss of GFP signal and increased cytotoxicity in response to DGAT1i plus erastin or RSL3 (Fig. 6c and Extended Data Fig. 8c). Both ferrostatin-1 and liproxstatin-1 attenuated this cytotoxicity, establishing ferroptosis as a major mechanism of cell death induced by combined disruption of LD buffering and SLC7A11 (Fig. 6d and Extended Data Fig. 8c). Although GFP-expression precluded direct analysis of lipid peroxidation in SB28-GFP spheroids, rescue of both cytotoxicity and lipid peroxidation by ferroptosis inhibitors was confirmed in U87MG cells (Extended Data Fig. 8d).

We next evaluated the therapeutic efficacy of combined DGAT1 and SLC7A11 inhibition in orthotopic SB28 tumours. To ensure sustained local drug exposure, we implanted micro-osmotic pumps 7 days after tumour cell injection to enable continuous intratumoral drug delivery for 14 days following initial tumour establishment (Fig. 6e and Extended Data Fig. 8e). Whereas neither DGAT1i nor erastin alone conferred any survival benefit, combined inhibition of DGAT1 and SLC7A11 significantly prolonged overall survival relative to controls (Fig. 6f). Together, these findings demonstrate that LD-mediated lipid buffering and SLC7A11-dependent antioxidant defence cooperate to protect tumour cells from ferroptotic collapse under necrotic lipid stress, and

287 that co-targeting these adaptive programs converts necrotic debris scavenging from a fitness
288 advantage into a therapeutically exploitable vulnerability *in vivo* (Fig. 6g).

Discussion

Tumour progression is driven by genetic diversification together with selection imposed by metabolic stress, immune surveillance and therapeutic pressure. Our findings identify necrosis as an additional selective force that actively shapes tumour evolution. Rather than representing a passive consequence of tissue destruction, necrotic regions constitute lipid-rich microenvironments that favour tumour cells capable of scavenging extracellular biomass, buffering lipid overload and engaging adaptive antioxidant programmes. In GBM, necrotic debris scavenging enhanced tumour fitness, including proliferation, radioresistance and tumorigenicity. These adaptations, however, came at the cost of an acquired dependence on coordinated lipid buffering and anti-ferroptotic mechanisms, thereby exposing a conditional metabolic vulnerability within the perinecrotic niche. Together, these findings establish necrosis as a dynamic ecological niche that simultaneously drives tumour adaptation and creates therapeutic opportunities.

Necrotic tissue clearance traditionally centres on the recruitment of professional phagocytes through damage-associated molecular patterns together with "find-me" and "eat-me" signals[32]. Increasing evidence, however, indicates that non-professional phagocytosis is a conserved property of tissue-resident cells, as recently demonstrated for hair follicle stem cells, contributing to tissue homeostasis[6]. Our findings extend this emerging concept from tissue homeostasis to cancer evolution by demonstrating that GBM cells themselves directly participate in necrotic biomass processing while shaping the recruitment and phenotype of professional phagocytes. Although the temporal dynamics remain unresolved, this reciprocal interaction suggests that necrosis establishes a self-reinforcing ecological circuit linking tumour adaptation with immune remodelling[21,33,34].

We further distinguish necrotic debris scavenging from previously described nutrient acquisition pathways. While macropinocytosis enables tumour cells to utilize extracellular macromolecules[4,5,9,19,35], necrotic debris presents the additional challenge of safely handling abundant membrane lipids and oxidizable fatty acids. Consistent with this complexity, NecD uptake displayed features of a regulated scavenging process, requiring intact NecD-associated protein ligands, cholesterol-rich membrane domains and dynamin, rather than classical bulk uptake[18,19,36]. These observations suggest that selective recognition of necrotic biomass serves not simply to acquire nutrients, but to enable controlled utilization of a uniquely complex metabolic resource.

LDs emerged as the central adaptive response to NecD scavenging, enabling GBM cells to channel excess fatty acids into neutral lipids while maintaining a metabolically accessible energy reservoir. Disrupting LD biogenesis abolished the growth-promoting and radioprotective effects of NecD scavenging, consistent with the increasingly recognized role of LDs in coordinating nutrient utilization, redox homeostasis and therapy resistance[12,15,16,37,38]. Our findings extend this concept by identifying LDs as dynamic organelles that permit continued exploitation of a nutrient-rich yet potentially toxic microenvironment.

Our data further support a hierarchical metabolic defence programme in which LD buffering constitutes the first line of protection against necrosis-derived lipid stress, while inducible antioxidant pathways provide a second compensatory layer when lipid sequestration is compromised. Importantly, LD disruption did not translate into meaningful cell death, indicating that LD buffering is necessary, but not sufficient, for full protection. Consistent with this model, anti-ferroptotic pathways centred around SLC7A11 and CPT1A were among the most consistently upregulated pathways following necrotic lipid overload, indicating that GBM cells dynamically

redistribute metabolic stress across complementary defence programmes. This adaptive hierarchy provides a mechanistic explanation for the pronounced therapeutic synergy observed upon combined inhibition of DGAT1 and SLC7A11. While neither intervention alone sufficiently compromised cell viability, simultaneous disruption of lipid buffering and glutathione-dependent antioxidant defence triggered extensive lipid peroxidation and cell death, which was rescued by ferroptosis inhibitors and lipid-soluble antioxidants[39]. Our findings identify SLC7A11-dependent cystine uptake as a key inducible defence against unresolved necrosis-derived lipid stress, consistent with its established role in cancer cell redox homeostasis[24]. Conversely, SLC7A11 inhibition may induce LD remodelling as a compensatory response[40], underscoring the close functional coupling between lipid buffering and antioxidant defence.

Our findings suggest that necrotic biomass establishes a conditional ferroptosis dependency by increasing reliance on coordinated lipid-buffering and redox defence systems. Such layered adaptation is likely advantageous within the fluctuating perinecrotic niche, where episodic exposure to necrotic biomass may generate recurrent cycles of lipid excess and oxidative stress. CPT1A induction may further contribute to this adaptation by facilitating metabolic handling of excess fatty acids, although its precise role remains to be determined. CPT1A supports GBM cell survival and stemness under metabolic stress[41,42], and inhibits ferroptotic lipid peroxidation[43,44]. Rather than relying on a single protective mechanism, tumour cells appear to engage an integrated network that preserves metabolic flexibility under changing environmental conditions. This layered logic parallels emerging observations across multiple tumour types that disrupting LD homeostasis sensitizes tumour cells to concomitant perturbation of antioxidant defence[45–47]. More broadly, our findings illustrate how adaptive metabolic programmes that initially promote tumour fitness can ultimately be converted into therapeutic liabilities, in line with growing interest in

leveraging ferroptosis induction for cancer therapy[48], including GBM where therapeutic translation will require brain permeable ferroptosis-inducing strategies[29,49].

Several questions arising from this work warrant further investigation. Our mechanistic analyses focused on SLC7A11 as the predominant inducible antioxidant defence engaged in response to necrosis-derived lipid stress, whereas the contribution of additional antioxidant pathways and their functional hierarchy remain to be defined. The phenocopy obtained with combined DGAT1 and GPX4 inhibition is consistent with the central, non-redundant role of GPX4 in restraining lethal lipid peroxidation[50]. Given that lipid peroxidation can propagate between neighbouring cells as self-amplifying oxidative trigger waves[51], it is tempting to speculate that combined disruption of lipid buffering and ferroptosis defence may extend beyond directly targeted cells, establishing a necrosis-lipid-ferroptosis amplification loop within the perinecrotic niche. Whether such bystander effects contribute to therapeutic efficacy *in vivo* remains an important question for future studies.

While multiple receptors have been implicated in the clearance of apoptotic debris, much less is known about the receptors and ligands governing necrotic debris scavenging[36]. Although our findings define a regulated scavenging process dependent on intact NecD-associated protein ligands, cholesterol-rich membrane domains and dynamin, consistent with receptor-mediated recognition, identification of the receptors and signalling pathways responsible for selective necrotic biomass uptake will be important for understanding how tumour cells compete for extracellular resources within the perinecrotic niche. From a therapeutic perspective, however, these mechanistic questions do not alter the central concept emerging from our study: the greatest vulnerability may not lie in preventing access to necrotic nutrients, but in disrupting the adaptive mechanisms that permit their safe utilization and tolerance to necrotic lipid overload.

In summary, our findings establish tumour necrosis as a metabolically active niche that supports tumour fitness through nutrient scavenging, metabolic adaptation and immune remodelling. At the same time, these adaptations create a dependence on coordinated lipid buffering and anti-ferroptosis defences. Thus, tumour exploitation of necrotic biomass transforms a defining pathological hallmark of aggressive cancers into a therapeutically exploitable metabolic vulnerability.

Main references

1. Quail, D. F. & Joyce, J. A. The microenvironmental landscape of brain tumors. *Cancer Cell* **31**, 326–341 (2017).

2. Markwell, S. M., Ross, J. L., Olson, C. L. & Brat, D. J. Necrotic reshaping of the glioma microenvironment drives disease progression. *Acta Neuropathol.* **143**, 291–310 (2022).

3. Greenwald, A. C. *et al.* Integrative spatial analysis reveals a multi-layered organization of glioblastoma. *Cell* **187**, 2485-2501.e26 (2024).

4. Commisso, C. *et al.* Macropinocytosis of protein is an amino acid supply route in Ras-transformed cells. *Nature* **497**, 633–637 (2013).

5. Finicle, B. T., Jayashankar, V. & Edinger, A. L. Nutrient scavenging in cancer. *Nat. Rev. Cancer* **18**, 619–633 (2018).

6. Stewart, K. S. *et al.* Stem cells tightly regulate dead cell clearance to maintain tissue fitness. *Nature* **633**, 407–416 (2024).

7. Bayona, C., Ranđelović, T. & Ochoa, I. Tumor microenvironment in glioblastoma: The central role of the hypoxic–necrotic core. *Cancer Lett.* **639**, 218216 (2026).

8. Corbet, C. & Feron, O. Tumour acidosis: from the passenger to the driver's seat. *Nat. Rev. Cancer* **17**, 577–593 (2017).

9. Jayashankar, V. & Edinger, A. L. Macropinocytosis confers resistance to therapies targeting cancer anabolism. *Nat. Commun.* **11**, 1121 (2020).

10. Scott, A. J. *et al.* Rewiring of cortical glucose metabolism fuels human brain cancer growth. *Nature* **646**, 413–422 (2025).

11. Dierge, E. *et al.* Peroxidation of n-3 and n-6 polyunsaturated fatty acids in the acidic tumor environment leads to ferroptosis-mediated anticancer effects. *Cell Metab.* **33**, 1701-1715.e5 (2021).

12. Dixon, S. J. & Olzmann, J. A. The cell biology of ferroptosis. *Nat. Rev. Mol. Cell Biol.* **25**, 424–442 (2024).

13. Wahida, A. & Conrad, M. Decoding ferroptosis for cancer therapy. *Nature Reviews Cancer 2025 25:12* **25**, 910–924 (2025).

14. Dai, E. *et al.* A guideline on the molecular ecosystem regulating ferroptosis. *Nat. Cell Biol.* **26**, 1447–1457 (2024).

15. Bång-Rudenstam, A. *et al.* Tumour acidosis remodels the glycocalyx to control lipid scavenging and ferroptosis. *Nat. Cell Biol.* **28**, 567–580 (2026).

16. Wei, R. & Petritsch, C. K. Lipid droplets as stress-buffering organelles in cancer cell homeostasis. *Commun. Biol.* **9**, 868 (2026).

17. Cheng, X. *et al.* Targeting DGAT1 ameliorates glioblastoma by increasing fat catabolism and oxidative stress. *Cell Metab.* **32**, 229-242.e8 (2020).

18. Wolfe, A. R. *et al.* Nutrient scavenging-fueled growth in pancreatic cancer depends on caveolae-mediated endocytosis under nutrient-deprived conditions. *Sci. Adv.* **10**, eadj3551 (2024).

19. Cerezo-Magaña, M., Christianson, H. C., van Kuppevelt, T. H., Forsberg-Nilsson, K. & Belting, M. Hypoxic induction of exosome uptake through proteoglycan-dependent endocytosis fuels the lipid droplet phenotype in Glioma. *Molecular Cancer Research* **19**, 528–540 (2021).

20. Xie, Y. *et al.* The Human Glioblastoma Cell Culture Resource: Validated Cell Models Representing All Molecular Subtypes. *EBioMedicine* **2**, 1351–1363 (2015).

21. Governa, V. *et al.* Protumoral lipid droplet-loaded macrophages are enriched in human glioblastoma and can be therapeutically targeted. *Sci. Transl. Med* **16**, eadk1168 (2024).

22. Paar, M. *et al.* Remodeling of Lipid Droplets during Lipolysis and Growth in Adipocytes. *Journal of Biological Chemistry* **287**, 11164–11173 (2012).

23. Mayer, N. *et al.* Development of small-molecule inhibitors targeting adipose triglyceride lipase. *Nat. Chem. Biol.* **9**, 785–787 (2013).

24. Koppula, P., Zhuang, L. & Gan, B. Cystine transporter SLC7A11/xCT in cancer: ferroptosis, nutrient dependency, and cancer therapy. *Protein Cell* **12**, 599–620 (2021).

25. Sato, H., Tamba, M., Ishii, T. & Bannai, S. Cloning and expression of a plasma membrane cystine/glutamate exchange transporter composed of two distinct proteins. *J. Biol. Chem.* **274**, 11455–11458 (1999).

26. Zhang, W., Liu, Y., Liao, Y., Zhu, C. & Zou, Z. GPX4, ferroptosis, and diseases. *Biomedicine & Pharmacotherapy* **174**, 116512 (2024).

27. Hangauer, M. J. *et al.* Drug-tolerant persister cancer cells are vulnerable to GPX4 inhibition. *Nature* **551**, 247–250 (2017).

28. Dixon, S. J. *et al.* Pharmacological inhibition of cystine-glutamate exchange induces endoplasmic reticulum stress and ferroptosis. *Elife* **3**, e02523 (2014).

29. Argenziano, M. G. *et al.* Emerging roles of ferroptosis in modulating the immune landscape of glial tumours. *Nat. Cell Biol.* **28**, 1364–1378 (2026).

30. Schlaepfer, I. R. & Joshi, M. CPT1A-mediated Fat Oxidation, Mechanisms, and Therapeutic Potential. *Endocrinology* **161**, bqz046 (2020).

31. Li, F. J. *et al.* System Xc −/GSH/GPX4 axis: An important antioxidant system for the ferroptosis in drug-resistant solid tumor therapy. *Front. Pharmacol.* **13**, 910292 (2022).

32. Westman, J., Grinstein, S. & Marques, P. E. Phagocytosis of Necrotic Debris at Sites of Injury and Inflammation. *Front. Immunol.* **10**, 3030 (2020).

33. Kloosterman, D. J. *et al.* Macrophage-mediated myelin recycling fuels brain cancer malignancy. *Cell* **187**, 5336-5356.e30 (2024).

34. Liu, M. *et al.* Spatial transcriptomics reveals segregation of tumor cell states in glioblastoma and marked immunosuppression within the perinecrotic niche. *Acta Neuropathol. Commun.* **12**, 64 (2024).

35. Davidson, S. M. *et al.* Direct evidence for cancer cell-autonomous extracellular protein catabolism in pancreatic tumors. *Nat. Med.* **23**, 235–241 (2017).

36. Schuermans, S., Kestens, C. & Marques, P. E. Systemic mechanisms of necrotic cell debris clearance. *Cell Death & Disease 2024 15:8* **15**, 557 (2024).

37. Vogel, F. C. E., Chaves-Filho, A. B. & Schulze, A. Lipids as mediators of cancer progression and metastasis. *Nat. Cancer* **5**, 16–29 (2024).

38. Zekanovic, S., Achaiber Sing, P., Leenstra, S. & Lamfers, M. L. M. Cut the fat: targeting cholesterol and lipid metabolism in glioblastoma. *Cell Death Dis.* **16**, 717 (2025).

39. Mishima, E. *et al.* Recommendations for robust and reproducible research on ferroptosis. *Nat. Rev. Mol. Cell Biol.* **26**, 615–630 (2025).

40. Rajput, D., Mahalingavelar, P., Soppina, V. & Kanvah, S. Improved lipophilic probe for visualizing lipid droplets in erastin-induced ferroptosis. *Org. Biomol. Chem.* **21**, 8554–8562 (2023).

41. Pike, L. S., Smift, A. L., Croteau, N. J., Ferrick, D. A. & Wu, M. Inhibition of fatty acid oxidation by etomoxir impairs NADPH production and increases reactive oxygen species resulting in ATP depletion and cell death in human glioblastoma cells. *Biochim. Biophys. Acta Bioenerg.* **1807**, 726–734 (2011).

42. Shim, J. K. *et al.* Etomoxir, a carnitine palmitoyltransferase 1 inhibitor, combined with temozolomide reduces stemness and invasiveness in patient-derived glioblastoma tumorspheres. *Cancer Cell Int.* **22**, 1–13 (2022).

43. Ma, L. *et al.* Targeting carnitine palmitoyl transferase 1A (CPT1A) induces ferroptosis and synergizes with immunotherapy in lung cancer. *Signal Transduct. Target. Ther.* **9**, 64 (2024).

44. Li, X. H. *et al.* CPT1A facilitated ferroptosis by forming feedback loop with Nrf2 via PI3K/AKT pathway in colorectal cancer. *Apoptosis* **30**, 2899–2915 (2025).

45. Pan, D. *et al.* DGAT1 Inhibition Induces Ferroptosis and Enhances Cancer Immunotherapy Efficacy. *Cancer Res.* **86**, 3026–3039 (2026).

46. Ferrada, L., Barahona, M. J., Vera, M., Stockwell, B. R. & Nualart, F. Dehydroascorbic acid sensitizes cancer cells to system xc- inhibition-induced ferroptosis by promoting lipid droplet peroxidation. *Cell Death Dis.* **14**, 637 (2023).

47. Wilcock, D. J. *et al.* Oxidative stress from DGAT1 oncoprotein inhibition in melanoma suppresses tumor growth when ROS defenses are also breached. *Cell Rep.* **39**, (2022).

48. Ubellacker, J. M. & Dixon, S. J. Prospects for ferroptosis therapies in cancer. *Nat. Cancer* **6**, 1326–1336 (2025).

49. Singh, S. *et al.* Harnessing ferroptosis to transform glioblastoma therapy and surmount treatment resistance. *Cell Death Discov.* **11**, 448 (2025).

50. Eaton, J. K. *et al.* Selective covalent targeting of GPX4 using masked nitrile-oxide electrophiles. *Nat. Chem. Biol.* **16**, 497–506 (2020).

51. Co, H. K. C., Wu, C. C., Lee, Y. C. & Chen, S. H. Emergence of large-scale cell death through ferroptotic trigger waves. *Nature* **631**, 654–662 (2024).

Methods

Compounds and antibodies

The following compounds were used: Cholera toxin subunit B-Alexa Fluor (AF) 488 (C34775), HCS LipidTOX green neutral lipid stain (H34475), HCS LipidTOX red neutral lipid stain (H34476), HCS LipidTOX deep red neutral lipid stain (H34477), Hoechst 33342 (1399), MitoTracker Red FM (M22425), BODIPY 581/591 C11 (D3861), BODIPY 500/510 C1,C12 (D3823), BODIPY 558/568 C12 (D3835), L-azidohomoalanine (C10102), palmitic acid azide (C10265), biotin-alkyne (B10185), Click-iT™ Cell Reaction Buffer Kit (C10269), Click-iT™ EdU Cell Proliferation for Imaging AF 488 (C10337), Click-iT™ EdU AF 488 Flow Cytometry Assay Kit (C10420), Click-iT™ Plus TUNEL Assay Kit AF 647 (C10619), all from Thermo Fisher Scientific; IncuCyte Cytotox Dyes (Green, 4632 and Red, 4633) from Sartorius; liproxstatin-1 (S7699) from Selleck Chemicals; ferrostatin-1 (SML0583), DGAT1 inhibitor A922500 (A1737), Fasnall benzenesulfonate salt/FASN inhibitor (SML1815), GSK2194069/fatty acid synthase (FASN) inhibitor (SML1259), alpha-tocopherol (T3634), dynasore monohydrate (D7693), methyl-β-cyclodextrin (C4555), EIPA (A3085), Rac1 inhibitor (553502), ATGL inhibitor atglistatin (SML1075), ACSL1 inhibitor Triacsin C (T4540), CPT1a inhibitor etomoxir (E1905), SLC7A11 inhibitor erastin (329600), GPX4 inhibitor RSL3 (SML2234), crystal violet (C0775), 3-(4,5-dimethyl-2-thiazolyl)-2,5-diphenyl-2H-tetrazolium bromide (MTT, M2128), cresyl violet (C5042), all from Sigma-Aldrich; CellTiter-Glo® cell viability assay (G4291) from Promega; FerroOrange (50-290-0934) from Dojindo Laboratories; M-CSF (216-MC/CF), GM-CSF (215-GM), all from R&D Systems.

The following antibodies were used: EEA1 (polyclonal, ab2900, IF (Immunofluorescence): 1:500), GLUT1 (clone EPR3915, ab115730, IF: 1:500); both from Abcam. Malondialdehyde

(clone 6H6, MA5-27559, IF: 1:100), SLC7A11 (clone A7C6-R, MA5-44922, IF: 1:200), and CPT1A (polyclonal, PA576788, IF: 1:200), from Invitrogen. Mouse F4/80 (clone Cl: A3-1, MCA497, IF: 1:20) from Biorad. PD-L1-APC (clone 29E.2A3, 329708, Flow Cytometry: 1:200;), from Biolegend.

The following secondary antibodies were used: Goat anti-mouse AF 488 (A1100, 1:500), AF 546 (A11030, 1:500), AF 647 (A21235, 1:500) or goat anti-rabbit AF 488 (A11008, 1:500), AF 546 (A11010, 1:500), AF 647 (A21244, 1:500); all from Invitrogen.

Streptavidin AF 488 (S32354, 1:500, Invitrogen) was used for labelling and imaging of biotinylated metabolites.

Human brain tumour sample collection and processing

Clinical specimens of viable tumour and necrotic tissue were collected from patients who underwent surgery at the Neurosurgery Department of Lund University Hospital, Sweden. The study was conducted according to the ICH/GCP guidelines, in agreement with the Helsinki Declaration, and approved by the local ethics committee of Lund University (Dnr. 454 2018/37). The inclusion criteria were age ≥ 18 years, WHO performance status 0-3, and ability to provide informed consent. No sex- or gender-related exclusion criteria were applied in this study, and participation was voluntary and without the provision of financial or other incentives. Patients were diagnosed through routine magnetic resonance imaging (MRI) of the brain, followed by standard surgical and pathological procedures. They received standard oncological treatment and appropriate follow-up in accordance with national recommendations. Tumour specimens from patients with glioma (WHO grade 2-4) were cryopreserved by snap-freezing in isopentane for subsequent immunohistochemistry and immunofluorescence (IF) evaluation. Fresh tumour tissue

was alternatively minced using a dissecting scalpel and subsequently dissociated with TrypLE Express (12605-010, Thermo Fisher Scientific) and deoxyribonuclease I (DNase I, 90083, Thermo Fisher Scientific) at 37°C for 20 min on an orbital shaker. The resulting cell suspension was filtered through 70- and 40-µm nylon cell filters, and red blood cells (RBCs) were eliminated using RBC lysis buffer (420301, BioLegend). Patient-derived cultures were allowed to adhere and were then fixed with 4% paraformaldehyde (PFA, J19943.K2, Thermo Fisher Scientific) prior to IF analysis.

Cell lines and patient-derived primary GBM cultures

U87MG human GBM (ATCC; HTB-14) and SB28 mouse GBM (DSMZ, ACC 880) cell lines were cultured in DMEM with high glucose (11551841, HyClone, GE Healthcare), supplemented with 10% (volume/volume) FBS (F7524, Sigma-Aldrich), 2 mmol/L L-glutamine, 100 U/mL penicillin, and 100 µg/mL Streptomycin (PEST, P0781, Sigma-Aldrich) for <30 passages. Patient-derived primary GBM cell cultures U3013MG, U3017MG, U3031MG, U3047MG, U3054MG, and U3065MG were acquired from the Human Glioma Cell Culture Biobank (HGCC), Uppsala[20], and cultured on poly-L-ornithine- (P3655, Sigma-Aldrich) and laminin- (L2020, Sigma-Aldrich) coated surfaces in serum-free Neurobasal : DMEM/F12 (1:1) medium (31331-093 and 21103-049, respectively, Gibco) supplemented with EGF (10 ng/mL), FGF (10 ng/mL) (AF-100-15 and 100-18B, respectively, Peprotech), and stem cell supplements N2 (17502-048, Gibco) and B27 (12587-010, Gibco), as described previously[20]. For spheroid cultures, HGCC cells were seeded at a density of 1.5 × 10^4 cells per well in PrimeSurface® 3D Culture Spheroid plates (Ultra Low Attachment, U-bottom 96-well plate, #MS-9096UZ, S-Bio) in their corresponding culture media and cultured on an orbital shaker at 90 rpm. After 10–14 days, spheroids reached a diameter of 0.4-0.6 mm, and the presence of a hypoxic and necrotic core was confirmed by a decreased nuclear density and

increased hypoxia marker GLUT1 expression at the spheroid core (Extended Data Fig. 1c). All cells were routinely grown in a humidified 21% O_2 and 5% CO_2 incubator at 37°C and routinely tested for Mycoplasma by DAPI staining and high-resolution confocal microscopy. For hypoxia experiments, cells were incubated in a humidified Sci-tive NN Hypoxia workstation set at 5% CO_2, 94% N_2, 1% O_2, and 37°C for indicated timepoints.

TCGA and IvyGap data retrieval

TPM normalized RNA sequencing data in The Cancer Genome Atlas (TCGA) (RRID:SCR_003193) GBM and LGG projects were retrieved using the TCGABiolinks R package (v2.38.0) and matched clinical annotations were retrieved from the GDC data portal. The updated IDH-mutation status / 1p19q codel statuses were retrieved from Ceccarelli and colleagues[52] (retrieval date 08-04-2026). FPKM normalized and log_2 transformed RNA sequencing data and matched clinical annotations for GBM patients in the Ivy Glioblastoma Atlas Project (IvyGap) (RRID: SCR_005044) were retrieved from the GlioVis portal (retrieval date 10-11-2025).

Necrotic debris preparation

To obtain necrotic cell debris, U87MG or SB28 cells were harvested, washed, resuspended in PBS at a concentration of 5–10 × 10^6 cells/mL, and subjected to five cycles of liquid nitrogen immersion (30 s) and thawing in a 37°C water bath, as previously described[53–55]. Necrotic cells were centrifuged at 10,000 × g, and the pelleted insoluble necrotic cell debris (hereafter referred to as NecD) was resuspended in appropriate serum-free culture medium before addition to recipient cells at the indicated cell ratios. Fresh patient tumour-derived necrotic tissue, identified intraoperatively as necrotic by neurosurgeons, was homogenised using a tissue homogeniser

(ULTRA-TURRAX T8, IKA) and pelleted at 10,000 × g to obtain a tumour-derived necrotic debris fraction (NecD-P). Alternatively, NecD-IR was generated by harvesting free-floating necrotic cells 72 h after exposure of U3017MG cells to a lethal irradiation dose of 60 Gy (XenX orthovoltage X-ray radiotherapy unit; Xstrahl Ltd., UK), and NecD-Starv following starvation of U3017MG or U3054MG cells in Neurobasal medium lacking supplements. Necrotic debris generation methods are summarised in Extended Data Fig. 1e. For NecD heat-denaturation, NecD preparations were incubated overnight at 56°C with agitation. For protein digestion, NecD preparations were incubated with 2.5 mg/mL trypsin (T4049, Sigma-Aldrich) or PBS as a control, overnight at 37°C with agitation, followed by three PBS washes to remove residual trypsin before use. NecD concentrations are defined in figures or figure legends as [x], representing the ratio of NecD cell equivalent per recipient cell (*e.g.*, for 20x, 1 recipient cell is treated with NecD generated from 20 cells). For NecD-P, relative cell equivalent was determined by weighting NecD-P pellet and comparing it to the weight of a known NecD quantity.

Metabolite tracking using click chemistry and BODIPY-DA

For metabolite tracking using click chemistry, GBM donor cells were loaded with L-azidohomoalanine (Ala, 25 μM) in methionine- and cysteine-free DMEM (21013024, Gibco), or with palmitic acid azide (PA, 25 μM) in full medium for 18 h, or with 5-ethynyl-2′-deoxyuridine (EdU, 100 μM) in full medium for 24 h. NecD was generated from azide-metabolite-loaded donor cells as described above. To assess scavenging of Ala and PA via labelled NecD, recipient cells were fixed, permeabilized with 0.1% saponin, blocked in 3% BSA, and copper-catalysed cycloaddition of azide metabolites to biotin-alkyne (B10185, Thermo Fisher Scientific) was performed using the Click-iT™ Cell Reaction Buffer Kit, followed by fluorescent staining 30 min

with 4 µg/mL streptavidin AF 488 (S32354, Invitrogen). Scavenging of EdU-labelled NecD was assessed using Cell Proliferation for Imaging AF 488 kit according to the manufacturer's instructions. Alternatively, lipid transfer was assessed by labelling donor cells with BODIPY-dodecanoic acid (BODIPY-DA) for 15 min at 37°C using BODIPY™ 500/510 C1,C12 (2.5 µM) or BODIPY™ 558/568 C12 (2.5 µM) before generation of BODIPY-DA-NecD.

Irradiation

Cells were irradiated at the indicated doses using a XenX orthovoltage X-ray radiotherapy unit (Xstrahl Ltd., UK) operated at 225 kV without a collimator. The dose rate corresponded to 19 s per Gy, with the gantry positioned at 0° and a source-to-target distance of 20 cm. Control (sham-irradiated) plates were placed in the irradiation room for an equivalent duration to control for time spent outside the incubator.

Laser-capture microdissection

Human GBM tumour cryosections (10 µm) were mounted on DNase- and RNase-free membranes (FrameSlidePET; Zeiss). Sections were stained for nuclei with cresyl violet and dehydrated in ice-cold ethanol. Adjacent sections were mounted on poly-L-lysine-coated slides and stained with Hoechst 33342, HCS LipidTOX green neutral lipid stain (LipidTOX green), and the macrophage marker CD68. CD68 was used to identify and exclude LD-loaded macrophages, as described previously[21]. CD68-negative tumour regions enriched for LDs (LD+) or lacking detectable LDs (noLD) were isolated by laser-capture microdissection (LCM) using a Zeiss PALM system. A ×5 objective was used to identify regions of interest and a ×20 objective for microdissection (n = 5 patients; total dissected area ~10 mm²). Microdissected regions were pooled by group and lysed in

50 µL lysis buffer within specialised AdhesiveCaps. RNA extraction, quality control and mRNA expression analyses are described in the Sample preparation for gene expression analysis section.

Cell treatments

Endocytosis inhibition: Cells were pre-treated with dynasore monohydrate (Dynasore, 20, 50 or 100 µM), methyl-β-cyclodextrin (MCD, 1, 2.5 or 5 µM), 5-(N-ethyl-N-isopropyl)amiloride (EIPA, 10 µM), or Rac1 inhibitor (100 µM) for 2 h for flow cytometry quantification, or overnight for confocal imaging, prior to NecD addition.

Inhibition of lipid metabolism: Cells were treated with fatty acid synthase (FASN) inhibitors Fasnall benzenesulfonate salt (Fasnall, 50 µM), or GSK2194069 (GSK219, 50 µM), DGAT1 inhibitor A922500 (DGAT1i, 20 or 40 µM), ATGL inhibitor atglistatin (ATGLi, 100 µM), or ACSL1 inhibitor Triacsin C (1 or 2.5 µM).

Modulation of lipid peroxidation and ferroptosis: Cells were treated with the SLC7A11 inhibitor erastin (25 µM), CPT1A inhibitor etomoxir (100 µM), or GPX4 inhibitor RSL3 (10 µM) alone or in combination with DGAT1i. Where indicated, cells were pre-treated with DGAT1i for 24 h before co-treatment with ferroptosis inducers. The antioxidants alpha-tocopherol (α-Toco, 100 µM), and anti-ferroptotic ferrostatin-1 (Fer-1, 1 µM) or liproxstatin-1 (Lip-1, 0.1 or 1 µM) were added concomitantly with ferroptosis inducers.

3D spheroid treatments: For spheroid experiments, cells were cultured for 7-10 days in PrimeSurface® 3D culture spheroid plates (S-Bio) prior to treatment initiation.

Treatment durations, concentrations, and culture conditions are provided in the corresponding figures and figure legends.

Proliferation and cell viability assays: Cells were washed with 1 M NaCl to remove residual surface-bound NecD, fixed, and stained with crystal violet (CV, 0.5%) in 20% methanol for 20 min following washing with water and air-drying. Culture plates were scanned using an Epson scanner, and CV was solubilized in 10% acetic acid for absorbance measurement at 590 nm using a spectrophotometer (FLUOstar OPTIMA, BMG Labtech). Alternatively, proliferating cells were quantified by EdU incorporation using the Click-iT™ EdU AF 488 Flow Cytometry Assay Kit. Cell viability and metabolic activity were assessed using the MTT assay, according to the manufacturer's recommendations. MTT absorbance was measured at 590 nm using a spectrophotometer. Intracellular ATP levels were quantified using the CellTiter-Glo® Cell Viability Assay according to the manufacturer's instructions and luminescence was measured using a luminometer (FLUOstar OPTIMA, BMG Labtech) with an integration time of 0.5-2 s.

LD formation assay

HGCC primary cells were cultured in their standard medium, while U87MG and SB28 cells were cultured in serum-free medium, with or without NecD at the indicated concentrations. When specified, cells were treated with DGAT1i or Triacsin C concomitantly with NecD, to inhibit triglyceride biosynthesis and LD formation, or with ATGLi (100 μM) after pre-incubation with NecD for inhibition of LD consumption. After 2-48 h, cells were washed with 1 M NaCl in PBS, fixed with 4% PFA for 10 min, and LDs were stained with LipidTOX green (1: 1,000 in PBS) for 30 min at room temperature (RT), followed by nuclear staining with Hoechst 33342 for 10 min. Imaging was performed on a Zeiss LSM980 confocal scanning system, as described under "Tissue and cell imaging" below.

683 **Tissue and cell imaging**

684 ***H&E staining:*** Cryosections were fixed in 4% PFA in PBS, washed in tap water, and stained with
685 Haematoxylin and Eosin solutions (01825 and 01650, Histolab). Sections were dehydrated through
686 graded alcohols (70%, 96%, and 100%) and incubated in xylene for 2 min before mounting (Pertex,
687 00801, Histolab) and imaging using an AxioScan.Z1 slide scanner (Zeiss).

688 ***IF staining:*** Human tumour and mouse brain cryosections (6 µm) from isopentane-cryopreserved
689 samples were rehydrated in PBS for 5 min, fixed in 4% PFA for 10 min at RT, and blocked with
690 5% normal goat serum (X0907, Dako/Agilent Technologies) in PBS for 1 h at RT. Spheroids were
691 collected after 14 days in culture, fixed in 4% PFA for 20 min at RT, incubated overnight in 0.5
692 M sucrose, embedded in Optimal Cutting Temperature compound (OCT, KMA-0100-00A,
693 CellPath), and cryosectioned (10 µm). PFA-fixed spheroid sections or two-dimensional cultures
694 were blocked with 3% BSA. For intracellular antigen detection, samples were permeabilised with
695 0.2% Triton X-100 for 10 min at RT. Primary antibodies diluted in blocking solution were
696 incubated overnight at 4°C, followed by incubation with AF-conjugated secondary antibodies
697 diluted in blocking solution for 1 h at RT. All antibodies and dilution factors are listed in the
698 section Compounds and antibodies.

699 LDs were stained with HCS LipidTOX neutral lipid stain (1:500) for 1 h at RT. Biotin-conjugated
700 metabolites were detected using streptavidin AF 488 for 1 h at RT. TUNEL staining was performed
701 using the Click-iT™ Plus TUNEL Assay Kit AF 647 according to the manufacturer's instructions.
702 Nuclei were counterstained with Hoechst 33342 for 10 min at RT. Samples were mounted in
703 fluorescent mounting medium (S3023, Dako/Agilent Technologies) prior to imaging. For
704 mitochondrial imaging, live cells were incubated with MitoTracker Red FM (250 nM) for 30 min
705 at 37°C. For labile iron imaging, live cells were incubated with FerroOrange (1 µM) for 30 min at

37°C. For lipid peroxidation analysis, live cells were incubated with BODIPY 581/591 C11 (BODIPY C11, 2.5 μM) for 6 h at 37°C. Cells were then washed and maintained in phenol-red-free medium (FluoroBrite™ DMEM, A18967-01, Thermo Fisher Scientific) for immediate imaging.

Within each experiment, all samples were imaged using identical acquisition settings. Three imaging instruments were used (all from Zeiss): An inverted Axio Observer Z.1 LSM 710 confocal laser scanning microscope equipped with Airyscan and photomultiplier tube (PMT) detectors, ×63/1.4 Plan-Apochromat and ×40/1.3 EC Plan-Neofluar oil-immersion objectives, and diode (405 nm), argon (488 nm), DPSS (561 nm), and HeNe (633 nm) lasers, operating under ZEN 2.1 (black); an inverted Axio Observer 7 LSM980 confocal laser scanning microscope, equipped with a 32-channel GaAsP spectral PMT detector, a ×63/1.40 C Plan-Apochromat oil-immersion lens, a ×40/1.20 C-Apochromat water-immersion objective lens, and diode lasers at 405 nm, 488 nm, 561 nm, and 633 nm, operating under ZEN 3.8.2 (blue); an Axio Scan.Z1 slide scanner, equipped with an Axiocam 506 camera, a ×20/0.8 M27 Plan-Apochromat objective lens, and a Colibri 5/7 LED light source, operating under ZEN 3.1 (blue). Image analyses were performed using Fiji (ImageJ software v1.54t). For fluorescence quantification, thresholded signal area or integrated density were normalised to the corresponding nuclear area within the same field, and mean fluorescence intensity (MFI) was measured from raw images. For quantification of F4/80-positive cells in necrotic versus viable SB28 tumour areas, necrotic regions were defined by reduced nuclear density and increased LD accumulation. LD area per cell was quantified by thresholding followed by particle analysis of LD-positive regions and nuclei counts.

Spheroid area quantification: Following the indicated treatments, 1.5 × 10^4 U87MG cells per well were plated in 96-well spheroid plates and cultured on an orbital shaker. After 48 h, spheroids

were imaged using a Zeiss PrimoVert microscope (4× objective). Images were converted to 8-bit grayscale, thresholded, and spheroid area was quantified using the Analyse Particles function in ImageJ.

Conditioned media collection

Conditioned medium (CM) was collected from cells cultured with or without NecD for 48 h. Cells were subsequently washed in 1 M NaCl to eliminate residual surface-bound NecD and incubated in fresh serum-free DMEM (for U87MG cells) or Neurobasal medium supplemented with N2 (for primary GBM cultures) for 24 h. CM was collected and centrifuged twice at 400 × g at 4°C to remove cell debris. Cleared CM was used immediately in subsequent experiments.

Macrophage isolation and polarization

Peripheral blood mononuclear cells (PBMCs) were isolated from leukocyte concentrates obtained from healthy donors through the Clinical Immunology and Transfusion Division (Skåne University Hospital) using Ficoll density gradient centrifugation. CD14+ monocytes were purified by positive magnetic selection using antibody-coated microbeads (130-050-20, Miltenyi Biotech) according to the manufacturer's instructions. Following isolation, monocytes were either used directly in migration assays or differentiated into macrophages by culture at 1 × 10^6 per mL in RPMI-1640 supplemented with 10% heat-inactivated FBS, 1% L-Glut, 1% PEST, and macrophage colony-stimulating factor (M-CSF, 15 ng/mL). Between days 3 and 7, half of the culture medium was replaced with fresh medium supplemented with M-CSF. On day 6, granulocyte–macrophage colony-stimulating factor (GM-CSF, 15 ng/mL) was added to support macrophage viability during subsequent experiments.

Flow cytometry analyses

Monocyte migration assay: CM collected from NecD-treated cells was added to 24-well plates. Primary monocytes isolated as described above were seeded at 1 × 10^6 cells per well in serum-free medium in the upper chamber of 3-µm-pore cell-culture inserts (Corning) placed above the CM. Monocytes were incubated for 2 h at 37 °C to allow migration towards CM from the indicated experimental conditions or medium supplemented with 2% FBS as a positive control. Migrated cells were collected from the lower chamber in 100 µL PBS and cell count was quantified using an Accuri C6 Flow Cytometer (BD Biosciences) by analysing identical volume (50 µL) from each sample.

Endocytosis assays: Cellular uptake activity was assessed by incubating adherent cells with CtxB-AF488 (5 µg/mL), for 1 h at 37°C or with BODIPY-DA-labelled NecD for 0.5-4 h (as indicated in the figure legends) at 37°C or 4°C, in serum-free DMEM (U87MG and SB28 cells) or complete primary cell medium (patient-derived GBM cultures). Following incubation, surface-bound signal was removed by washing in 1 M NaCl before cell detachment with trypsin (U87MG and SB28) or TrypLE Express (patient-derived GBM cultures). Cellular fluorescence was quantified as MFI using an Accuri C6 Flow Cytometer and analysed with BD CSampler Plus software v1.0.27.1 (BD Biosciences).

Macrophage analyses: Human primary macrophages were detached using Accutase (25-058-CI, Corning), resuspended in FACS buffer (PBS, 0.5% FBS, and 2 mM EDTA), and blocked with 5% human serum (S1-M, Sigma-Aldrich) or 3% BSA in PBS for 15 min at RT. Cells were stained for 15 min at 4°C with fluorophore-conjugated mouse monoclonal antibody against PD-L1 (anti-PD-L1-APC), washed in FACS buffer, and centrifuged at 300-400 × g for 5 min at 4°C. Samples were

acquired on a BD FACSDiscover™ S8 Cell Sorter flow cytometer (BD Biosciences) and analysed using FlowJo software (BD Biosciences).

IncuCyte live-cell analysis

Live monitoring of 3D spheroid growth, LD accumulation, cytotoxicity, and lipid peroxidation was performed using an IncuCyte S3 live-cell analysis system (Sartorius), housed in a humidified incubator at 37°C and 5% CO_2. Spheroids were generated by seeding 1.5 × 10^4 cells per well in 96-well U-bottom spheroid plates and treated 7-10 days after spheroid formation, as described in the Cell treatments section.

To assess cytotoxicity, spheroids were treated in the presence of IncuCyte Cytotox Green Dye (250 nM) or IncuCyte Cytotox Red Dye (250 nM). Lipid peroxidation was monitored by addition of BODIPY 581/591 C11 (2.5 μM) to the culture medium, and LD accumulation was assessed using LipidTOX Green (1: 1,000). One image per well was acquired every 2-3 h from treatment initiation for up to 7 days.

Image acquisition, analysis and visualisation were performed using IncuCyte integrated software (v2022B Rev2 or v2024B), with identical analysis settings applied across all images intended for comparison. For statistical analyses, each well was considered an independent data point. Spheroid size was quantified as total brightfield object area (μm^2). Cytotoxicity was quantified as the MFI or integrated fluorescence intensity of the largest brightfield object following top-hat background subtraction. Lipid peroxidation was calculated as the ratio of oxidised BODIPY signal (green fluorescence intensity) to reduced BODIPY signal (red fluorescence intensity) within the same spheroid following top-hat background subtraction. Data are presented as fold change relative to

the indicated reference condition at the selected time points specified in the figures or figure legends.

Mouse models

Experiments involving orthotopic GBM allograft and xenograft models were approved by the Ethical Committee for Animal Research in Lund-Malmö (permit numbers 5.8.18-14006/2019 and 5.8.18-01073/2024) and performed in accordance with Swedish national regulations and European Union directives governing animal welfare. Mice were housed in a specific pathogen-free facility under a 12-h light/dark cycle with *ad libitum* access to food and water, ambient temperature of 20-26 °C, and relative humidity of 30-70%. Animals were monitored daily and euthanised upon signs of neurological distress.

For the syngeneic GBM model, 1.6 × 10^3 SB28 cells (control or NecD-pre-conditioned) were orthotopically implanted into the brains of 5-7-week-old female C57BL/6J mice (The Jackson Laboratory, JAX) in 4 µL serum-free medium. For the human xenograft model, 1 × 10^5 U87MG cells (control or NecD-pre-conditioned) were orthotopically implanted into 5-7-week-old male and female NOD SCID gamma (NSG) mice (JAX) in 4 µL serum-free medium supplemented with 10% Growth Factor Reduced Matrigel (354230, Corning). Mice were anaesthetised with isoflurane and positioned in a stereotactic frame. Cells were injected into the right striatum, 1 mm anterior and 2.5 mm lateral to bregma, and 2.5 mm below the dural surface. Mice bearing U87MG xenografts were euthanised at a pre-defined time-point (21 days after implantation). In the SB28 model, the primary endpoint was overall survival (OS).

For treatment studies, drugs were delivered continuously into the tumour through a mini-osmotic pump connected to an intracranial catheter inserted via the original burr hole at day 7 following

tumour cell injection, at which time-point SB28 tumour establishment had been confirmed by bioluminescence imaging (IVIS Spectrum imaging system, PerkinElmer)[56,57]. Mini-osmotic pumps (Alzet model 1002; 14-day delivery) containing vehicle (artificial cerebrospinal fluid, aCSF; 3525, Bio-Techne), DGAT1i (80 μM), erastin (50 μM), or a combination of both agents, were implanted subcutaneously under anaesthesia. At the end of the treatment period (14 days), pumps were removed under general anaesthesia. The primary endpoint was OS, with 9-11 mice per treatment group. Following euthanasia, brains were dissected and snap-frozen in isopentane for cryopreservation and further analysis.

Transcriptomics

Primary GBM cells were seeded in T25 flasks and treated with NecD and/or DGAT1i for 48 h, and in indicated cases, cells were then irradiated with 2 Gy and incubated for another 6 h, followed by 1 M NaCl wash and sample collection in RNeasy Lysis Tissue (RLT) buffer. Total RNA from these samples and samples from microdissected tissue, as described above, was isolated using the AllPrep DNA/RNA Micro Kit (80284, Qiagen) according to the manufacturer's instructions. RNA concentration and purity were determined using BioAnalyzer to ascertain acceptable RNA Integrity Number (RIN) values (RIN was ≥ 9.9 for all samples), and mRNA expression was analysed using an Affymetrix Clariom D Pico Gene Array that generates robust expression profiles down to 100 pg of total RNA (BEA core Facility, Karolinska Institute, Stockholm, Sweden).

Gene Array processing and NecD-Induced transcriptional signature generation

Raw probe intensities from the Affymetrix gene array experiments were background corrected, normalized, and summarized to gene-level expression values using the Signal Space

Transformation-Robust Multichip Analysis (SST-RMA) algorithm on the Transcriptome Analysis Console (TAC, v4.0.3.14, ThermoFisher Scientific). All downstream processing and analysis of the normalized expression values from TAC were performed using R (v4.5.3) within RStudio. Probe IDs were annotated with the affycoretools (v1.80.0) package using the clariomdhumantranscriptcluster.db (v8.8.0) annotation data package. The data was filtered to retain only protein-coding genes based on probe annotations. The expression values were $\log_2$ transformed and differential expression analysis was performed between all relevant contrast groups using the limma (v3.64.3)[58] package by fitting a linear model to compute coefficient estimates and their standard errors. Empirical Bayes moderation was applied to generate moderated t- and F-statistics and the log-odds of differential expression. Benjamini-Hochberg (BH) multiple testing correction was applied and significantly differentially expressed genes were identified. The NecD-induced transcriptional signature was defined as the 28 top genes showing significantly increased expression ($\log_2$FC > 1, FDR < 0.05) in NecD-treated compared to untreated control.

Quantitative real-time PCR

Primary GBM cell cultures treated with NecD and/or DGAT1i were collected in RLT buffer, and total RNA was extracted using the GenElute Mammalian Total RNA Miniprep Kit (RTN70, Sigma-Aldrich) according to the manufacturer's protocol. RNA concentration was determined using a spectrophotometer (DeNovix DS-11). cDNA was synthesised using the SuperScript III First-Strand Synthesis System kit (11752, Thermo Fisher Scientific) with random hexamer primers on a MasterCycler EpGradient 5341 thermal cycler (Eppendorf). Real-time qPCR was performed on a StepOnePlus Real-Time PCR System (Applied Biosystem) using SYBR Green JumpStart

Taq Readymix (S4438, Sigma-Aldrich). All reactions were performed in triplicate, with n = 3 biological replicates. Gene expression was normalised to the GAPDH housekeeping gene, and relative expression was calculated using the comparative Ct method (2^−ΔΔCt). The primers (Thermo Fisher Scientific) were designed as follows: IL1B: F: 5′-ATGAAGTGCTCCTTCCAGGAC-3′, R: 5′-TGTCCATGGCCACAACAACT-3′; SLC7A11: F: 5′-CAAATGCAGTGGCAGTGACC-3′, R: 5′-CAGCAAACACACCACCGTTC-3′; CPT1A: F: 5′-ATGTACGCCAAGATCGACCC-3′, R: 5′-TGACCACGTTCTTCGTCTGG-3′; and GAPDH (glyceraldehyde 3-phosphate dehydrogenase): F: 5′-GAAGGTGAAGGTCGGAGTCAAC-3′, R: 5′-CAGAGTTAAAAGCAGCCCTGGT-3′.

NecD-induced signature scoring and TCGA survival analysis

NecD-induced gene signature scores for patients in the IvyGap and TCGA GBM/LGG cohorts were calculated as normalized enrichment scores from single-sample gene set enrichment analysis (ssGSEA) using the GSVA (v2.2.1) R package. For the TCGA GBM survival analysis, patients were stratified into NecD signature –High and –Low groups based on whether the patient's NecD signature score was in the top or bottom 20% of all patients in the TCGA GBM data.

Pathway analysis

Gene set enrichment analysis (GSEA)[59] was performed using the clusterProfiler (v4.16.0)[60] package, against pathway gene sets from Kyoto Encyclopedia of Genes and Genomes (KEGG), Gene Ontology Biological Processes (GO:BP), Hallmark, and WikiPathways retrieved from the Molecular Signatures Database (MSigDB, release 2024.1)[61], and against GBM subtype signature gene sets from Wang and colleagues[62]. GSEA was also performed against gene sets generated

from published and validated ferroptosis driver and suppressor genes retrieved from FerrDB V3[63], and filtered to retain genes with more than one publication implicating them as either a suppressor or driver (Score > 1), and only those with rigorous experimental validation involving pharmacological or genetic inhibition or activation assays (Confidence = "Validated"). The $\log_2$ fold change values were used as the ranking metric for the input gene lists and the resulting p-values were adjusted for multiple testing with BH correction.

Software, statistics and reproducibility

The software used for individual analyses is described above in the respective sections. R (v4.5.3) with RStudio and GraphPad Prism (v11.0.2) were used to create figures and perform statistical testing. Schematic illustrations were created using BioRender.com, and the figure composition was performed using Adobe Illustrator v.30.5.

GSEA statistics for Enrichment score (ES), Normalized Enrichment Score (NES), nominal p-value, and FDR were performed in R using the clusterProfiler (v4.14.4) R package. Significance tests of differentially expressed genes were performed on $\log_2$-transformed expression values using moderated t statistics as per the limma package. Comparisons of tumour region (IvyGap) means were performed with Wilcoxon signed-rank test. Statistical analyses of quantitative experimental models were performed using an unpaired Student's t-test (two-tailed) for two-group comparisons. Multiple group comparisons were performed by one-way ANOVA with Tukey´s *post hoc* test (or two-stage step-up method of Benjamini Kruger and Yekutieli to correct for False Discovery Rate), or two-way ANOVA with Tukey's post hoc test. For survival curves, *p* values were obtained using the log-rank (Mantel-Cox) test. *In vitro* experiments were performed with at least three independent biological replicates in a minimum of two independent experiments, unless otherwise

stated in the figure legends. Both technical and biological replicates were found to be reproducible. Data are represented as mean ± s.e.m., with *$P \leq 0.05$, **$P \leq 0.01$, ***$P \leq 0.001$, and ‡FDR ≤ 0.05, ‡‡FDR ≤ 0.01, ‡‡‡FDR ≤ 0.001.

Sample size determination

Sample sizes are similar to those reported in previous publications[15,19,21,64,65]. No statistical methods were used to predetermine sample sizes.

Data exclusion

No data were excluded from the analyses.

Randomization

For *in vitro* studies, the experiments were not randomised; however, all cell lines/spheroids were treated identically without prior designation. For *in vivo* mouse experiments involving NecD pre-conditioning or drug treatment, same-aged female mice were randomly assigned to experimental groups, anonymised, and distributed in mixed cages for blinded survival analysis.

Blinding

Data collection and analysis were not performed blind to the conditions of the experiments, except for *in vivo* survival analysis (Fig. 2n and 6f).

Assumptions for statistical test

Data distribution was assumed to be normal, but this was not formally tested.

Data and code availability

All data and software used in this study are, or will be, publicly available prior to publication through publicly maintained repositories and licensed vendors. LCM mRNA array data (Fig. 2b) is available in the NCBI Gene Expression Omnibus (GEO) under accession codes GSE300758, and the newly generated mRNA array datasets will be deposited prior to publication. All other materials are available on request from the corresponding author.

Acknowledgments

We thank all the patients that contributed to this study. We are grateful to all members of the Belting group for input during manuscript preparation. This work was supported by grants from the Swedish Cancer Society, CAN 23 2655 Pj (to M.B.), the Swedish Research Council, VR-MH 2023-02106 (to M.B.), the Swedish Childhood Cancer Foundation, PR2023-0078 (to M.B.), the Fru Berta Kamprad Foundation (to M.B.), governmental funding of clinical research within the national health services, ALF (to M.B.), and a generous donation by Viveca Jeppsson (to M.B. and J.B.).

Author contributions

H.T. and M.C.M. acquired FACS, confocal microscopy, cell proliferation, metabolic, and radioresistance studies, and H.T. acquired Incucyte data. V.G., with support from E.H., generated laser capture microdissection transcriptomics data. H.T. and M.C.M, with support from V.G., generated U3017MG transcriptomics data, E.H. performed all related transcriptomics analysis in cell models and patient cohorts, and A.B. performed RT-qPCR. V.G. and F.T., with support from H.T, performed monocyte and macrophages experiments. H.T., E.G., S.J., D.T. and A.B.R.

performed animal studies, and S.B.B. performed *in vivo* imaging. H.T., D.T., and S.B., sectioned human and mice tumour samples, and spheroids, and acquired scanner microscopy images, J.B., with support from C.E., provided patient tumour materials. A.D., R.M., and S.J. provided *in vivo* experimental expertise. H.T., M.C.M and M.B. wrote the manuscript. M.B. conceived and supervised the study. H.T. and M.B. designed the study and experiments. All authors edited and approved the manuscript.

Competing interests

The authors declare no competing interests.

Inclusion & Ethics

The study involved human tissue specimens and patient-derived cell cultures obtained with informed consent and under protocols approved by institutional review boards. All animal experiments were performed in compliance with institutional and national ethical guidelines, with approval from the appropriate animal care and use committees (see Methods). This work reflects a collaborative effort, and all contributors are appropriately acknowledged. The authors are committed to principles of inclusion, equity, and transparency, and will make all relevant data and materials available in accordance with *Nature's* policies.

Corresponding authors Correspondence to: mattias.belting@med.lu.se and hugo.talbot@med.lu.se

Methods references

52. Ceccarelli, M. *et al.* Molecular Profiling Reveals Biologically Discrete Subsets and Pathways of Progression in Diffuse Glioma. *Cell* **164**, 550–563 (2016).

53. Trusal, L. R., Guzman, A. W. & Baker, C. J. Characterization of freeze-thaw induced ultrastructural damage to endothelial cells in vitro. *In Vitro* **20**, 353–364 (1984).

54. Eigenbrod, T., Park, J.-H., Harder, J., Iwakura, Y. & Núñez, G. Critical Role for Mesothelial Cells in Necrosis-Induced Inflammation through the Recognition of IL-1α Released from Dying Cells. *Journal of immunology* **181**, 8194–8198 (2008).

55. Katakam, S., Anand, S., Martin, P., Riggi, N. & Stamenkovic, I. Necrotic debris and STING exert therapeutically relevant effects on tumor cholesterol homeostasis. *Life Sci. Alliance* **5**, e202101256 (2022).

56. Bata Gouda, M. H., Cordella, C. B. Y. & Duarte-Sierra, A. The IVIS imaging system: Principle, performance, applications and perspectives in postharvest research. *Prog. Biophys. Mol. Biol.* **200**, 19–30 (2026).

57. Taş, İ. *et al.* Advanced organoid models for targeting Kras-driven lung adenocarcinoma in drug discovery and combination therapy. *Journal of Experimental and Clinical Cancer Research* **44**, 128 (2025).

58. Phipson, B., Lee, S., Majewski, I. J., Alexander, W. S. & Smyth, G. K. Robust hyperparameter estimation protects against hypervariable genes and improves power to detect differential expression. *Ann. Appl. Stat.* **10**, 946 (2016).

59. Subramanian, A. *et al.* Gene set enrichment analysis: A knowledge-based approach for interpreting genome-wide expression profiles. *Proc. Natl. Acad. Sci. U. S. A.* **102**, 15545–15550 (2005).

60. Xu, S. *et al.* Using clusterProfiler to characterize multiomics data. *Nat. Protoc.* **19**, 3292–3320 (2024).

61. Liberzon, A. *et al.* The Molecular Signatures Database Hallmark Gene Set Collection. *Cell Syst.* **1**, 417–425 (2015).

62. Wang, Q. *et al.* Tumor Evolution of Glioma-Intrinsic Gene Expression Subtypes Associates with Immunological Changes in the Microenvironment. *Cancer Cell* **32**, 42-56.e6 (2017).

63. Zhou, N. *et al.* FerrDb V3: expanding the manually curated resource for regulators and disease associations from ferroptosis to regulated cell death. *Nucleic Acids Res.* **54**, D572–D582 (2026).

64. Menard, J. A. *et al.* Metastasis Stimulation by Hypoxia and Acidosis-Induced Extracellular Lipid Uptake Is Mediated by Proteoglycan-Dependent Endocytosis. *Cancer Res.* **76**, 4828–4840 (2016).

65. Christianson, H. C., Svensson, K. J., Van Kuppevelt, T. H., Li, J. P. & Belting, M. Cancer cell exosomes depend on cell-surface heparan sulfate proteoglycans for their internalization and functional activity. *Proc. Natl. Acad. Sci. U. S. A.* **110**, 17380–17385 (2013).

Fig. 1

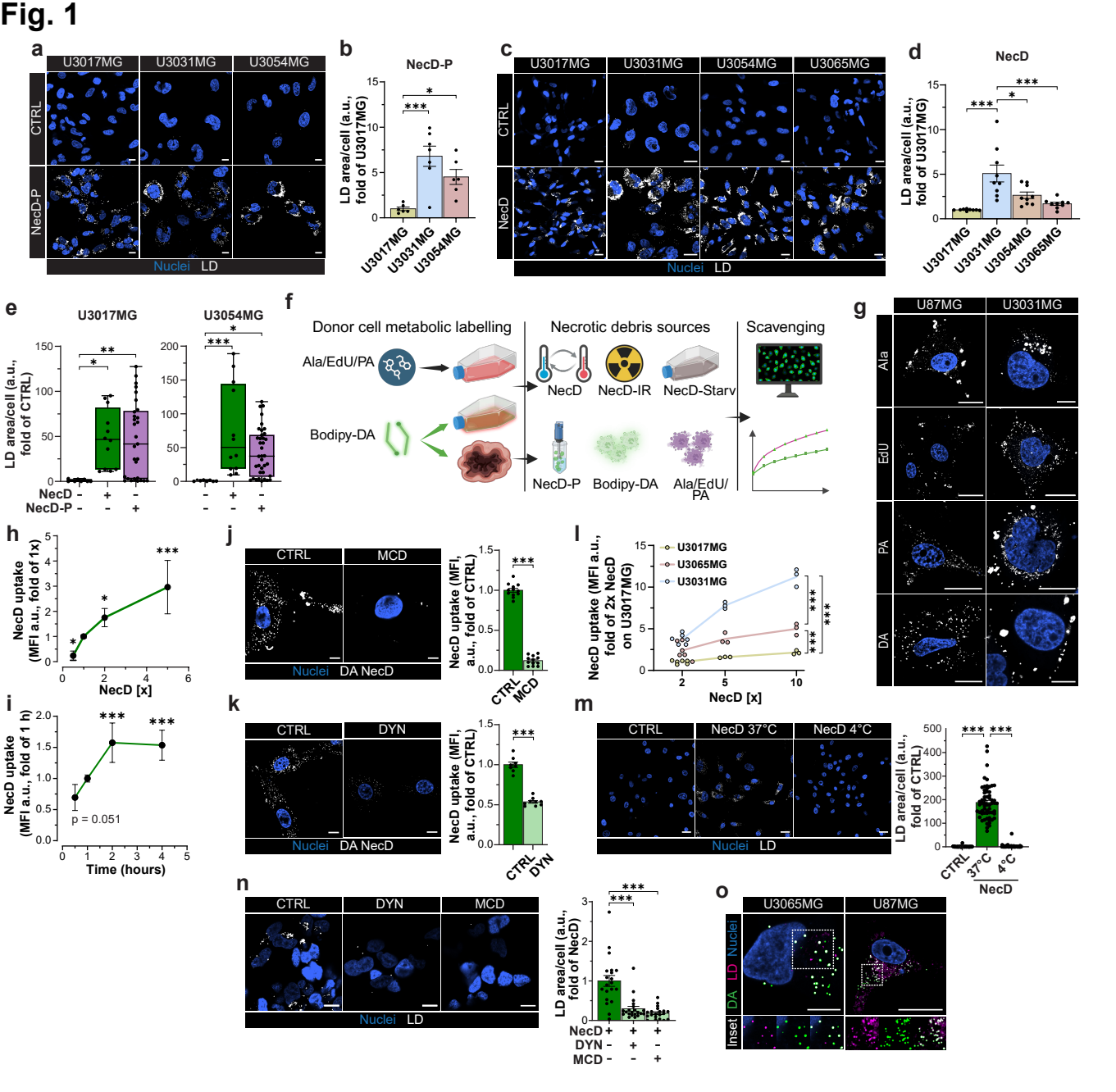

a
U3017MG
U3031MG
U3054MG
CTRL
NecD-P
Nuclei LD
b
NecD-P
LD area/cell (a.u., fold of U3017MG)
c
U3017MG
U3031MG
U3054MG
U3065MG
CTRL
NecD
Nuclei LD
d
NecD
e
U3017MG
U3054MG
LD area/cell (a.u., fold of CTRL)
NecD
NecD-P
f
Donor cell metabolic labelling
Necrotic debris sources
Scavenging
Ala/EdU/PA
Bodipy-DA
NecD
NecD-IR
NecD-Starv
NecD-P
Bodipy-DA
Ala/EdU/ PA
g
U87MG
U3031MG
Ala
EdU
PA
DA
h
NecD uptake (MFI a.u., fold of 1x)
NecD [x]
i
NecD uptake (MFI a.u., fold of 1 h)
p = 0.051
Time (hours)
j
CTRL
MCD
Nuclei DA NecD
NecD uptake (MFI, a.u., fold of CTRL)
k
CTRL
DYN
Nuclei DA NecD
NecD uptake (MFI, a.u., fold of CTRL)
l
NecD uptake (MFI a.u., fold of 2x NecD on U3017MG)
U3017MG
U3065MG
U3031MG
NecD [x]
m
CTRL
NecD 37°C
NecD 4°C
Nuclei LD
LD area/cell (a.u., fold of CTRL)
37°C
4°C
NecD
n
CTRL
DYN
MCD
Nuclei LD
LD area/cell (a.u., fold of NecD)
NecD
DYN
MCD
o
U3065MG
U87MG
Nuclei
LD
DA
Inset

Fig. 1 GBM cells scavenge necrotic debris for lipid buffering. a and **b,** Fluorescence imaging (**a**; representative of $n > 5$ NecD-P samples) and quantification (**b**) of LDs in U3017MG, U3031MG, and U3054MG cells treated with or without 20x NecD-P for 48 h (mean fold of U3017MG untreated control (CTRL) ± s.e.m., $n \geq 3$ areas per condition, from 2 independent NecD-P samples). **c, d,** Fluorescence imaging (**c**; representative of ≥ 3 independent experiments) and quantification (**d**) of LDs in U3017MG, U3031MG, U3054MG, and U3065MG treated with or without 20x NecD for 48 h (mean fold of U3017MG CTRL ± s.e.m., $n = 9$ areas per condition, from 3 independent experiments). **e,** Quantification of LD area per cell in U3017MG (left) and U3054MG (right) treated with or without 20x NecD or NecD-P for 48 h (mean fold of untreated control ± s.e.m., $n \geq 3$ areas per condition, from 3 independent experiments, and 8 independent NecD-P samples). **f,** Metabolic labelling strategy used to trace NecD-derived macromolecule uptake. **g,** Fluorescence imaging of metabolite-labelled NecD uptake for 2 h in U87MG and U3031MG cells (representative of ≥ 3 independent experiments). **h** and **i,** Flow cytometry quantification of NecD uptake in U87MG according to NecD concentration (**h**; NecD cell equivalent per recipient cell [x]; mean fold of 1x NecD ± s.e.m., $n = 9$ from 3 independent experiments; statistical comparison to 1x NecD group) and uptake time (**i**; mean fold of 1 h ± s.e.m., $n = 6$ from 2 independent experiments; statistical comparison to the 1 h group). **j,** Fluorescence imaging (left, representative of 3 independent experiments) and flow cytometry quantification (right, mean fold of untreated control ± s.e.m., $n = 12$ from 4 independent experiments) of Bodipy-DA labelled NecD uptake for 1 h in U87MG, with or without 2.5 μM methyl-β-cyclodextrin (MCD). **k,** Fluorescence imaging (left, representative of 3 independent experiments) and flow cytometry quantification (right, mean fold of untreated control ± s.e.m., $n = 9$ from 3 independent experiments) of Bodipy-DA labelled NecD uptake in U87MG for 1 h,

with or without 50 μM Dynasore. **l,** Flow cytometry quantification of Bodipy-DA labelled NecD uptake for 2 h in U3017MG, U3031MG and U3065MG according to NecD concentration (mean fold of 2x NecD in U3017MG ± s.e.m., $n \geq 3$ biological replicates). **m,** Fluorescence imaging (left, representative of 3 independent experiments) and quantification (right, mean fold of untreated control (no NecD) ± s.e.m., $n \geq 40$ images per condition, from 3 independent experiments) of LDs in U87MG with or without 20x NecD for 3 h, at 37°C or 4°C. **n,** Fluorescence imaging (left, representative of 2 independent experiments) and quantification (right, mean fold of NecD ± s.e.m., $n \geq 20$ images per condition, from 2 independent experiments) of LD formation in U3017MG with 20x NecD for 24 h following 2 h pretreatment and continuous treatment with Dynasore (20 μM) or MCD (5 μM). **o,** Fluorescence imaging of Bodipy-DA labelled NecD uptake after 4 h and LD formation (LipidTox, magenta) in U3065MG and U87MG (representative of 2 independent experiments). Significance was determined by one-way ANOVA (**b,d,e,h,i,m,n**), two-way ANOVA (**l**) or two-sided unpaired *t*-test (**j,k**). Scale bars 10 μm (**a,c,g,o**), 5 μm (**j,k**), and 20 μm (**m,n**).

Fig. 2

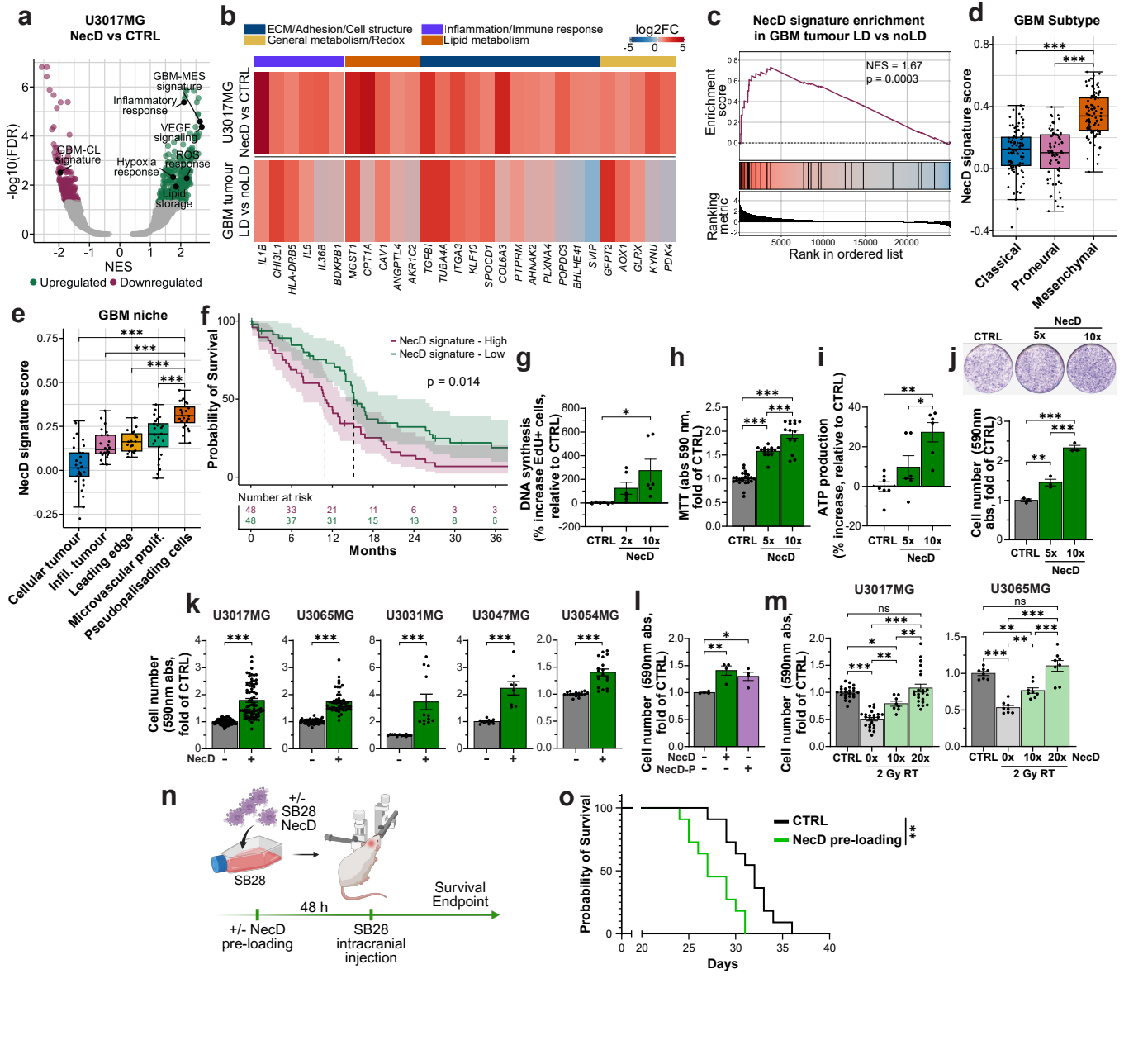

a
U3017MG
NecD vs CTRL
GBM-MES signature
Inflammatory response
VEGF signaling
ROS response
Hypoxia response
GBM-CL signature
Lipid storage
-log10(FDR)
NES
Upregulated
Downregulated
b
ECM/Adhesion/Cell structure
General metabolism/Redox
Inflammation/Immune response
Lipid metabolism
log2FC
U3017MG NecD vs CTRL
GBM tumour LD vs noLD
IL1B
CHI3L1
HLA-DRB5
IL6
IL36B
BDKRB1
MGST1
CPT1A
CAV1
ANGPTL4
AKR1C2
TGFBI
TUBA4A
ITGA3
KLF10
SPOCD1
COL6A3
PTPRM
AHNAK2
PLXNA4
POPDC3
BHLHE41
SVIP
GFPT2
AOX1
GLRX
KYNU
PDK4
c
NecD signature enrichment in GBM tumour LD vs noLD
Enrichment score
NES = 1.67
p = 0.0003
Ranking metric
Rank in ordered list
d
GBM Subtype
NecD signature score
Classical
Proneural
Mesenchymal
e
GBM niche
NecD signature score
Cellular tumour
Infil. tumour
Leading edge
Microvascular prolif.
Pseudopalisading cells
f
NecD signature - High
NecD signature - Low
p = 0.014
Probability of Survival
Number at risk
Months
g
DNA synthesis (% increase EdU+ cells, relative to CTRL)
CTRL
2x
10x
NecD
h
MTT (abs 590 nm, fold of CTRL)
CTRL
5x
10x
NecD
i
ATP production (% increase, relative to CTRL)
CTRL
5x
10x
NecD
j
CTRL
NecD
5x
10x
Cell number (590nm abs, fold of CTRL)
CTRL
5x
10x
NecD
k
U3017MG
U3065MG
U3031MG
U3047MG
U3054MG
Cell number (590nm abs, fold of CTRL)
NecD
l
Cell number (590nm abs, fold of CTRL)
NecD
NecD-P
m
U3017MG
U3065MG
Cell number (590nm abs, fold of CTRL)
CTRL
0x
10x
20x
2 Gy RT
NecD
n
+/- SB28 NecD
SB28
48 h
Survival Endpoint
+/- NecD pre-loading
SB28 intracranial injection
o
Probability of Survival
CTRL
NecD pre-loading
Days

Fig. 2. Necrotic debris scavenging promotes GBM fitness. a, Volcano plot of enriched pathways (NES, normalized enrichment score; FDR < 0.05) from transcriptomic profiling of U3017MG treated with 20x NecD for 48 h versus untreated controls (n = 3 biological replicates per condition). **b,** Heatmap of NecD transcriptional signature genes robustly upregulated ($log_2FC > 1$, FDR < 0.05) in NecD-treated versus untreated (CTRL) U3017MG cells (top, n = 3 biological replicates per condition) and the corresponding signature in LD-rich (LD) versus LD-negative (noLD) GBM tumour regions captured by laser-capture microdissection (LCM) (bottom, n = 5 patients). **c,** GSEA enrichment plot of the NecD signature in LD versus noLD GBM tumour regions (n = 5 patients). **d,** ssGSEA scores of the NecD transcriptional signature across GBM transcriptional subtypes from Ivy GAP (n = 122; boxes represent the interquartile range, the central line indicates the median, and whiskers represent the upper and lower quartiles). **e,** ssGSEA scores of the NecD transcriptional signature across GBM histological regions from Ivy GAP (n = 122). **f,** Kaplan-Meier survival curves of patients with primary GBM (IDHwt, 1p19q non-codeleted) from the TCGA-GBM cohort (n = 239) stratified by high (upper 20^{th} percentile) versus low (lower 20^{th} percentile) NecD signature expression. **g,** Flow cytometry quantification of EdU incorporation in U87MG cells after 24 h treatment with the indicated NecD concentrations (mean percentage increase relative to untreated control ± s.e.m., n = 6 from 3 independent experiments). **h,** MTT assay of U87MG cells treated with the indicated NecD concentrations for 48 h (mean fold of untreated control ± s.e.m., $n \geq 14$ from 3 independent experiments). **i,** Quantification of ATP production in U87MG cells after 48 h treatment with the indicated NecD concentrations (mean percentage increase relative to untreated control ± s.e.m., $n \geq 7$ from 2 independent experiments). **j,** Representative crystal violet staining after 48 h incubation with the indicated NecD concentrations (top) and corresponding quantification (bottom) in U87MG (mean fold of untreated

control ± s.e.m., n = 3 biological replicates). **k,** Crystal violet quantification of cell number in U3017MG, U3065MG, U3031MG, U3047MG and U3054MG after 96 h treatment with 20x NecD (mean fold of untreated control ± s.e.m.; $n \geq 73$ biological replicates from 16 independent experiments, $n \geq 45$ biological replicates from 11 independent experiments, $n \geq 12$ biological replicates from 3 independent experiments, $n \geq 8$ biological replicates from 2 independent experiments and $n \geq 17$ biological replicates from 4 independent experiments for U3017MG, U3065MG, U3031MG, U3047MG and U3054MG, respectively). **l,** Crystal violet quantification of cell number in U3017MG after 96 h treatment with 20x NecD or NecD-P (mean fold of untreated control ± s.e.m., n = 4 biological replicates). **m,** Crystal violet quantification of U3017MG (left; $n \geq 22$ biological replicates from 5 independent experiments, except for 10× NecD, n = 8 biological replicates from 2 independent experiments) and U3065MG (right; n = 8 biological replicates from 2 independent experiments) 72 h after 2 Gy irradiation, following 24 h pretreatment and continuous treatment with the indicated NecD concentrations (mean fold of untreated control ± s.e.m.). **n,** Experimental design for orthotopic implantation of SB28 cells pretreated with or without 20x NecD for 48 h. **o,** Kaplan-Meier survival curves of mice orthotopically implanted with parental (control) or NecD-preconditioned SB28 cells (n = 11 mice per group). Significance was determined using the Benjamini-Hochberg-adjusted nominal p-value (**a,c**), Wilcoxon rank-sum test (**e**), log-rank (Mantel-Cox) (**f,o**), one-way ANOVA (**g,h,i,j,k,l,m**), or two-sided unpaired t-test (**d**).

Fig. 3

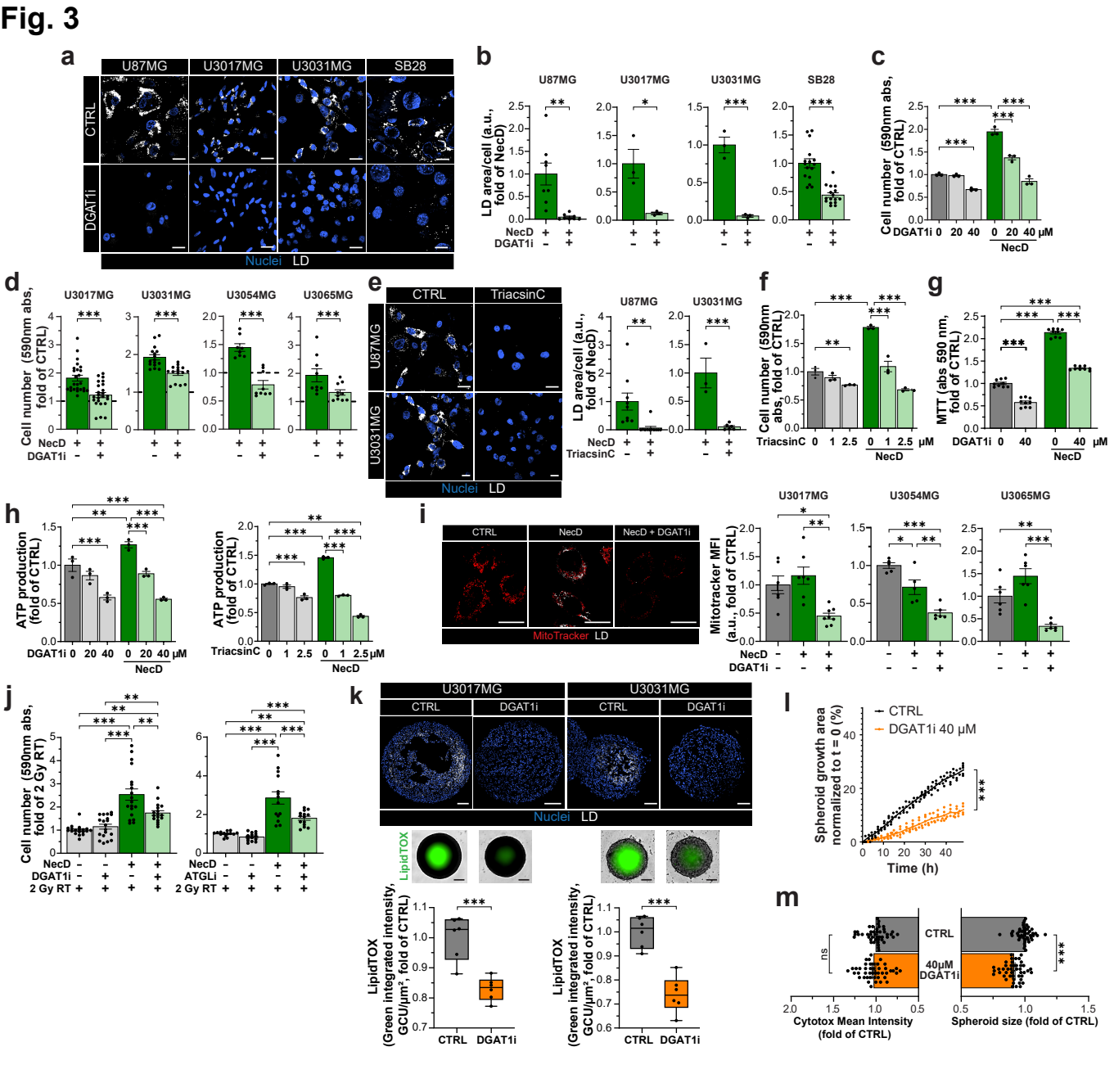

a
U87MG
U3017MG
U3031MG
SB28
CTRL
DGAT1i
Nuclei LD
b
U87MG
U3017MG
U3031MG
SB28
LD area/cell (a.u., fold of NecD)
NecD
DGAT1i
c
Cell number (590nm abs, fold of CTRL)
DGAT1i 0 20 40 0 20 40 µM
NecD
d
U3017MG
U3031MG
U3054MG
U3065MG
Cell number (590nm abs, fold of CTRL)
NecD
DGAT1i
e
CTRL
TriacsinC
U87MG
U3031MG
Nuclei LD
LD area/cell (a.u., fold of NecD)
NecD
TriacsinC
f
Cell number (590nm abs, fold of CTRL)
TriacsinC 0 1 2.5 0 1 2.5 µM
NecD
g
MTT (abs 590 nm, fold of CTRL)
DGAT1i 0 40 0 40 µM
NecD
h
ATP production (fold of CTRL)
DGAT1i 0 20 40 0 20 40 µM
NecD
ATP production (fold of CTRL)
TriacsinC 0 1 2.5 0 1 2.5 µM
NecD
i
CTRL
NecD
NecD + DGAT1i
MitoTracker LD
U3017MG
U3054MG
U3065MG
Mitotracker MFI (a.u., fold of CTRL)
NecD
DGAT1i
j
Cell number (590nm abs, fold of 2 Gy RT)
NecD
DGAT1i
2 Gy RT
NecD
ATGLi
2 Gy RT
k
U3017MG
U3031MG
CTRL
DGAT1i
Nuclei LD
LipidTOX
LipidTOX (Green integrated intensity, GCU/µm², fold of CTRL)
CTRL DGAT1i
l
CTRL
DGAT1i 40 µM
Spheroid growth area normalized to t = 0 (%)
Time (h)
m
CTRL
40µM DGAT1i
ns
Cytotox Mean Intensity (fold of CTRL)
Spheroid size (fold of CTRL)

Fig. 3. LD biogenesis underpins NecD-induced tumour fitness but is dispensable for survival. **a** and **b**, Fluorescence imaging (**a**) and quantification (**b**) of LDs in U87MG, U3017MG, U3031MG and SB28 48 h after incubation with 20x NecD, with or without treatment with 40 μM DGAT1i (mean fold of untreated control ± s.e.m., $n \geq 3$ areas per condition). **c**, Crystal violet quantification of U87MG cell number after 48 h treatment with or without 20x NecD and DGAT1i as indicated (mean fold of untreated control ± s.e.m., $n = 3$ biological replicates). **d**, Crystal violet quantification of cell number in U3017MG, U3031MG, U3054MG and U3065MG following 96 h treatment with or without 20x NecD and 40 μM DGAT1i (mean fold of untreated control without NecD ± s.e.m., $n \geq 9$, from 5, 4, 2 and 2 independent experiments for U3017MG, U3031MG, U3054MG and U3065MG, respectively). **e**, Fluorescence imaging (left) and quantification (right) of LDs in U87MG and U3031MG 48 h after incubation with 20x NecD, with or without treatment with Triacsin C (1 μM for U3031MG and 2.5 μM for U87MG) (mean fold of untreated control ± s.e.m., $n \geq 3$ areas per condition). **f**, Crystal violet quantification of U87MG cell number after 48 h treatment with or without 20x NecD and Triacsin C as indicated (mean fold of untreated control ± s.e.m., $n = 3$ biological replicates). **g**, MTT assay of U87MG after 48 h treatment with or without 20x NecD and DGAT1i as indicated (mean fold of untreated control ± s.e.m., $n = 9$ from 3 independent experiments). **h**, Quantification of ATP production in U87MG after 48 h treatment with or without 20x NecD and DGAT1i (left) or Triacsin C (right) as indicated (mean fold of untreated control ± s.e.m., $n = 3$ biological replicates). **i**, Fluorescence imaging of LDs and mitochondrial integrity assessed by MitoTracker Red (left; U3054MG) and quantification of MitoTracker fluorescence intensity (right) in U3017MG, U3054MG and U3065MG treated with or without 20x NecD and 40 μM DGAT1i for 48 h (mean fold of untreated control ± s.e.m., $n \geq 5$ areas per condition). **j**, Crystal violet quantification of U3017MG cell number 72 h after 2 Gy

irradiation, following 24 h pretreatment and continuous treatment with or without NecD and 40 μM DGAT1i (left; added simultaneously with NecD) or 100 μM ATGLi (right; added at the time of irradiation) (mean fold of untreated control ± s.e.m., $n \geq 14$ from 4 and 3 independent experiments, respectively). **k**, Fluorescence imaging of LDs in cryosections of U3017MG and U3031MG spheroids (top) and representative IncuCyte images (middle) with quantification (bottom) of LipidTOX accumulation (bottom; mean fold of untreated control ± s.e.m., $n = 6$ spheroids per condition) following 48 h treatment with or without 40 μM DGAT1i. **l**, Spheroid size over time determined by IncuCyte live-cell imaging of U3017MG spheroids treated as in **k** (mean fold of untreated control ± s.e.m., $n = 6$ spheroids per condition). **m**, Quantification of cytotoxicity and spheroid size following 48 h treatment with or without 40 μM DGAT1i, determined by IncuCyte live-cell imaging (mean fold of untreated control ± s.e.m., $n = 45$ spheroids per condition from 9 independent experiments). Significance was determined by two-sided unpaired *t*-test (**b**,**d**,**e**,**k**,**m**), one-way ANOVA (**c**,**f,g,h,i,j**), or two-way ANOVA (**l**). Scale bars, 20 μm (**a**,**e**,**i**), 100 μm (**k, top**) and 200 μm (**k, middle**).

Fig. 4

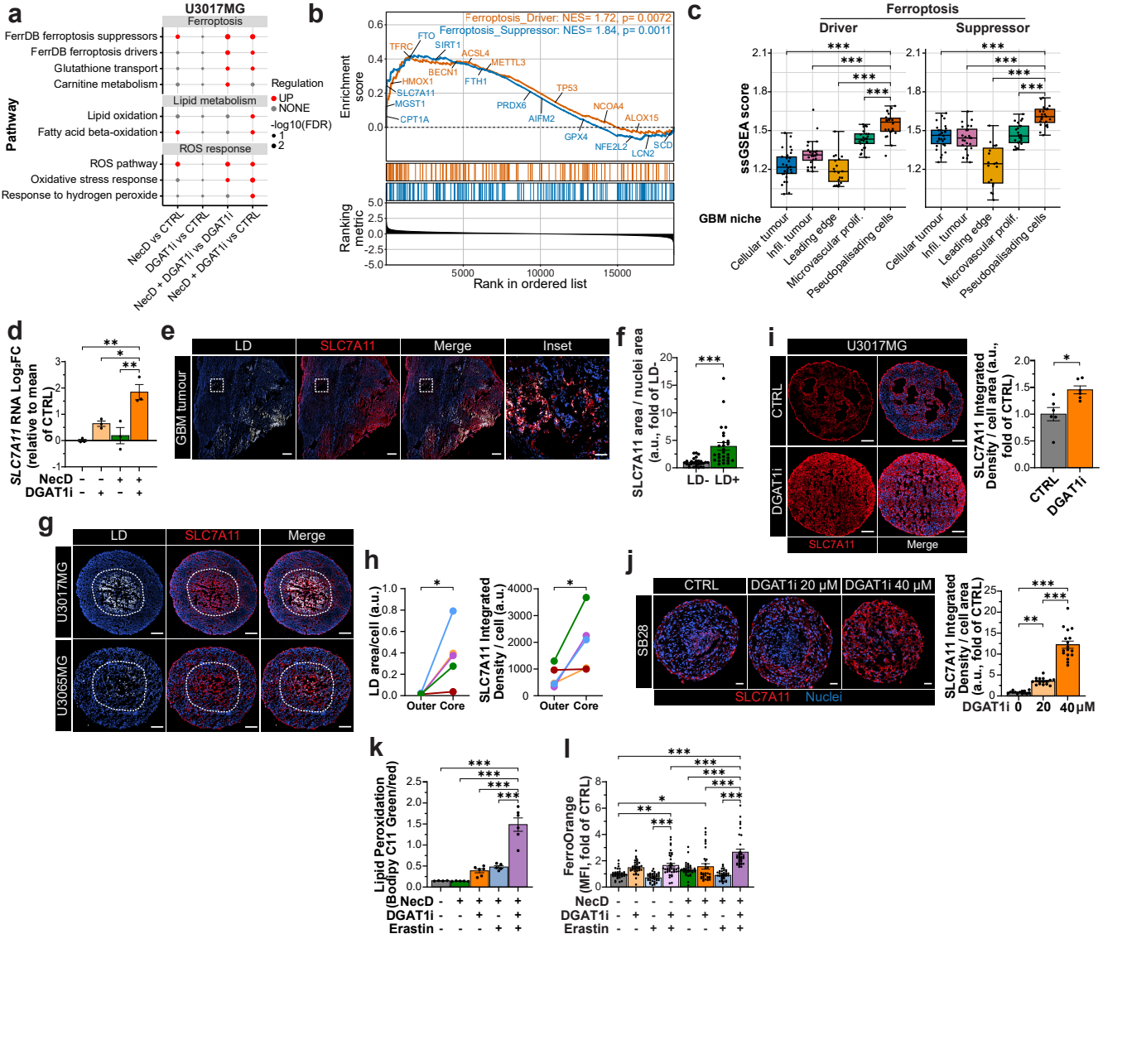

a
U3017MG
Ferroptosis
FerrDB ferroptosis suppressors
FerrDB ferroptosis drivers
Glutathione transport
Carnitine metabolism
Lipid metabolism
Lipid oxidation
Fatty acid beta-oxidation
ROS response
ROS pathway
Oxidative stress response
Response to hydrogen peroxide
Pathway
Regulation
UP
NONE
-log10(FDR)
1
2
NecD vs CTRL
DGAT1i vs CTRL
NecD + DGAT1i vs DGAT1i
NecD + DGAT1i vs CTRL
b
Ferroptosis_Driver: NES= 1.72, p= 0.0072
Ferroptosis_Suppressor: NES= 1.84, p= 0.0011
Enrichment score
TFRC
FTO
SIRT1
ACSL4
METTL3
BECN1
FTH1
HMOX1
SLC7A11
MGST1
CPT1A
PRDX6
TP53
NCOA4
AIFM2
ALOX15
GPX4
NFE2L2
LCN2
SCD
Ranking metric
Rank in ordered list
c
Ferroptosis
Driver
Suppressor
ssGSEA score
GBM niche
Cellular tumour
Infil. tumour
Leading edge
Microvascular prolif.
Pseudopalisading cells
d
SLC7A11 RNA Log2FC (relative to mean of CTRL)
NecD
DGAT1i
e
LD
SLC7A11
Merge
Inset
GBM tumour
f
SLC7A11 area / nuclei area (a.u., fold of LD-)
LD-
LD+
i
U3017MG
CTRL
DGAT1i
SLC7A11
Merge
SLC7A11 Integrated Density / cell area (a.u., fold of CTRL)
g
LD
SLC7A11
Merge
U3017MG
U3065MG
h
LD area/cell (a.u.)
SLC7A11 Integrated Density / cell (a.u.)
Outer Core
j
CTRL
DGAT1i 20 μM
DGAT1i 40 μM
SB28
SLC7A11
Nuclei
SLC7A11 Integrated Density / cell area (a.u., fold of CTRL)
DGAT1i 0 20 40μM
k
Lipid Peroxidation (Bodipy C11 Green/red)
NecD
DGAT1i
Erastin
l
FerroOrange (MFI, fold of CTRL)
NecD
DGAT1i
Erastin

Fig. 4. Disruption of NecD-induced lipid buffering activates compensatory anti-ferroptotic programs. a, Selected enriched pathways (FDR < 0.05) identified by GSEA of transcriptomic profiles from U3017MG treated for 48 h with or without 20x NecD and 40 μM DGAT1i. **b,** GSEA enrichment plot of "Ferroptosis_Driver" and "Ferroptosis_Suppressor" signatures in U3017MG treated as in **a**. The ten highest-ranked ferroptosis driver and suppressor genes (FerrDb v3), together with selected genes of interest, are indicated. **c,** ssGSEA scores of ferroptosis driver and suppressor signatures across GBM histological regions from Ivy GAP (n = 122). **d,** *SLC7A11* expression in U3017MG treated as in **a** (log2 fold change relative to untreated control ± s.e.m., n = 3 biological replicates). **e,** Fluorescence imaging of LDs and SLC7A11 in human GBM tumour sections (representative of 3 tumours). **f,** Quantification of SLC7A11 staining in LD-negative (LD-) versus LD-high (LD+) regions of GBM tumours stained as in **e** (mean fold of LD- regions ± s.e.m., n = 27 paired LD- and LD+ regions from 3 tumours). **g,** Fluorescence imaging of LDs and SLC7A11 in U3017MG and U3065MG spheroid sections (representative of 5 spheroids, dashed lines indicate necrotic core). **h,** Quantification of LDs (left) and SLC7A11 (right) in core regions and outer regions of U3017MG spheroids stained as in **g** (matched LD area per cell or SLC7A11 integrated density per cell, n = 5 spheroids). **i,** Fluorescence imaging in U3017MG spheroids (left) and quantification (right) of SLC7A11 staining after 48 h treatment with or without 40 μM DGAT1i (mean fold of CTRL ± s.e.m., from $n \geq 14$ spheroids per condition). **j,** Fluorescence imaging (left), and quantification (right) of SLC7A11 staining in SB28 spheroids after 48 h treatment with or without DGAT1i (mean fold of untreated control ± s.e.m., from n = 6 spheroids). **k,** Quantification of cellular lipid peroxidation, measured as the ratio of oxidized to reduced C11-BODIPY581/591 fluorescence intensity by live-cell imaging (representative images in **Extended Data Fig. 6f**) of U3065MG cells pre-treated with or without NecD for 48 h followed by erastin

1157 treatment for 6 h (mean Bodipy ratio ± s.e.m., n ≥ 4 images per condition). **l,** Quantification of
1158 cellular Fe^{2+}, measured by FerroOrange staining in live-cell imaging (representative images in
1159 **Extended Data Fig. 6g**) of U3017MG cells pre-treated with or without NecD for 48 h followed
1160 by Erastin for 4h (mean C11-BODIPY ratio ± s.e.m., n ≥ 34 images per condition from 2
1161 independent experiments). Significance was determined by Benjamini-Hochberg -adjusted
1162 nominal *p*-value (**a,b**), Wilcoxon rank-sum test (**c**), two-sided unpaired *t*-test (**f,h,i**), or one-way
1163 ANOVA (**d,j,k,l**). Scale bars 1,000 μm (**e**), 100 μm (**g,i**) and 50 μm (**e** inset, **j**).

Fig. 5

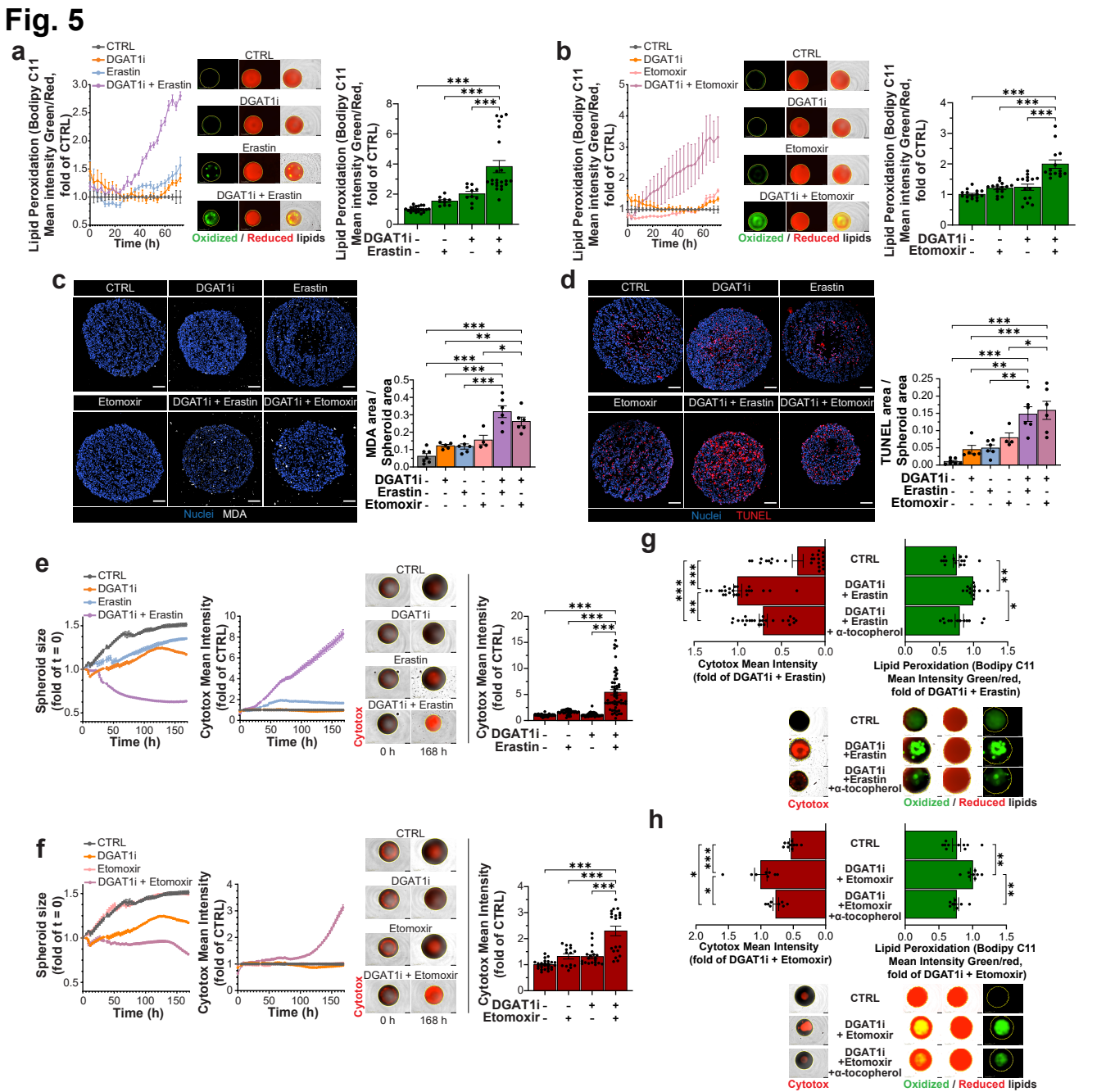

a
CTRL
DGAT1i
Erastin
DGAT1i + Erastin
Lipid Peroxidation (Bodipy C11 Mean intensity Green/Red, fold of CTRL)
Time (h)
Oxidized / Reduced lipids
DGAT1i
Erastin
b
Etomoxir
DGAT1i + Etomoxir
Etomoxir
c
Etomoxir
DGAT1i + Erastin
DGAT1i + Etomoxir
Nuclei MDA
MDA area / Spheroid area
d
Nuclei TUNEL
TUNEL area / Spheroid area
e
Spheroid size (fold of t = 0)
Cytotox Mean Intensity (fold of CTRL)
Cytotox
0 h
168 h
f
g
Cytotox Mean Intensity (fold of DGAT1i + Erastin)
Lipid Peroxidation (Bodipy C11 Mean Intensity Green/red, fold of DGAT1i + Erastin)
+ α-tocopherol
h
Cytotox Mean Intensity (fold of DGAT1i + Etomoxir)
Lipid Peroxidation (Bodipy C11 Mean Intensity Green/red, fold of DGAT1i + Etomoxir)

Fig. 5. Co-targeting LD buffering and adaptive anti-ferroptotic programs induces oxidative lipid stress and GBM cell death. a, Live-cell imaging based quantification of lipid peroxidation over time (left) in U3017MG spheroids treated with or without 40 μM DGAT1i and 25 μM erastin ($n = 5$ spheroids from one representative experiment), together with representative images (middle) and quantification (right) after 72 h (mean fold of untreated control ± s.e.m., $n \geq 10$ spheroids per condition from 4 (control and DGAT1i + erastin) or 2 (DGAT1i and erastin) independent experiments). **b,** Lipid peroxidation analyses as in (**a**) with or without 40 μM DGAT1i and 100 μM etomoxir (mean fold of untreated control ± s.e.m., $n \geq 14$ spheroids per condition from 3 independent experiments). **c** and **d,** Fluorescence imaging (left), and quantification (right) of MDA (**c**) and TUNEL (**d**) staining in U3065MG spheroids treated for 7 days with or without 40 μM DGAT1i, 25 μM erastin, or 100 μM etomoxir as indicated (mean ± s.e.m., $n \geq 4$ spheroids per condition). **e,** Live-cell imaging based quantification of spheroid size (left) and cytotoxicity (middle left) over time in U3017MG spheroids treated with or without 40 μM DGAT1i and 25 μM erastin (mean fold of $t = 0$ and untreated control ± s.e.m. respectively, from $n = 5$ spheroids from one representative experiment, with representative images (middle right), together with endpoint quantification (right) after 120 h (mean fold of untreated control ± s.e.m., $n \geq 38$ spheroids per condition from $n \geq 8$ independent experiments). **f,** Spheroid size and cytotoxicity analyses as in (**e**) with or without 40 μM DGAT1i and 100 μM etomoxir (mean fold of untreated control ± s.e.m., $n \geq 14$ spheroids per condition from $n \geq 3$ independent experiments). **g,** Live-cell imaging-based quantification of cytotoxicity (top left) and lipid peroxidation (top right) in U3017MG spheroids treated with or without 40 μM DGAT1i, 25 μM erastin, and 100 μM α-tocopherol, together with representative images (bottom) after 120 h (mean fold of DGAT1i + Erastin ± s.e.m., $n \geq 29$ or $n \geq 13$ spheroids from 6 and 3 independent experiments for cytotoxicity and lipid peroxidation,

respectively). **h,** Cytotoxicity and lipid peroxidation analyses as in (**g**) treated with or without 40 μM DGAT1i, 100 μM etomoxir, and 100 μM α-tocopherol (mean fold of DGAT1i + Etomoxir ± s.e.m., $n \geq 8$ from 2 independent experiments). Significance was determined by one-way ANOVA (**a,b,c,d,e,f,g,h**). Scale bars 400 μm (**a,b,e,f,g,h**) and 100 μm (**c,d**).

Fig. 6

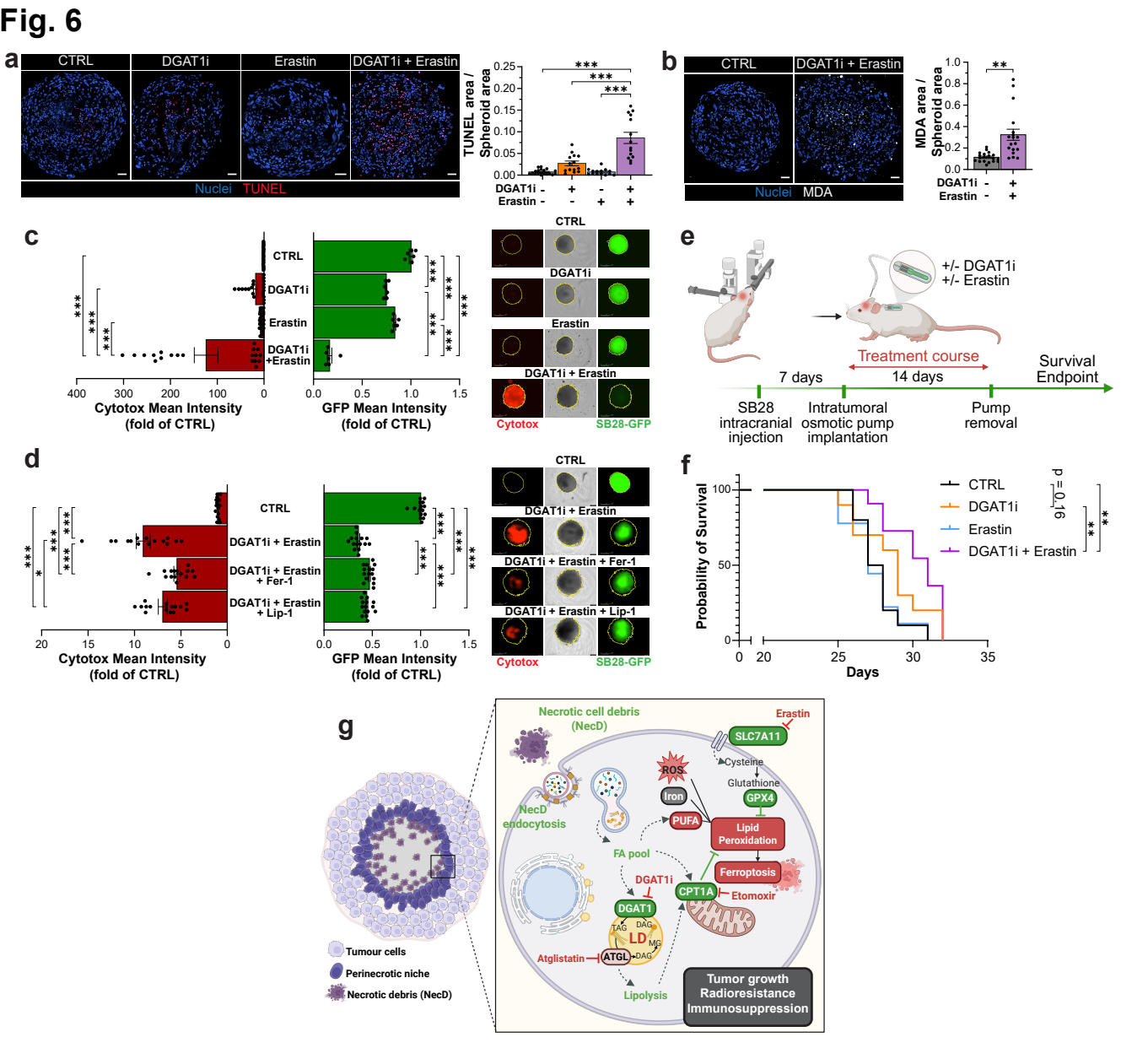

a
CTRL
DGAT1i
Erastin
DGAT1i + Erastin
Nuclei TUNEL
TUNEL area / Spheroid area
DGAT1i
Erastin
b
CTRL
DGAT1i + Erastin
Nuclei MDA
MDA area / Spheroid area
c
CTRL
DGAT1i
Erastin
DGAT1i +Erastin
Cytotox Mean Intensity (fold of CTRL)
GFP Mean Intensity (fold of CTRL)
Cytotox
SB28-GFP
d
CTRL
DGAT1i + Erastin
DGAT1i + Erastin + Fer-1
DGAT1i + Erastin + Lip-1
Cytotox Mean Intensity (fold of CTRL)
GFP Mean Intensity (fold of CTRL)
e
+/- DGAT1i
+/- Erastin
Treatment course
7 days
14 days
Survival Endpoint
SB28 intracranial injection
Intratumoral osmotic pump implantation
Pump removal
f
Probability of Survival
Days
CTRL
DGAT1i
Erastin
DGAT1i + Erastin
p = 0.16
g
Necrotic cell debris (NecD)
Erastin
SLC7A11
Cysteine
Glutathione
GPX4
ROS
Iron
PUFA
Lipid Peroxidation
NecD endocytosis
FA pool
Ferroptosis
DGAT1i
CPT1A
Etomoxir
DGAT1
TAG
DAG
LD
MG
Atglistatin
ATGL
DAG
Lipolysis
Tumor growth
Radioresistance
Immunosuppression
Tumour cells
Perinecrotic niche
Necrotic debris (NecD)

Fig. 6. Combined targeting of LD buffering and SLC7A11 exposes a therapeutic vulnerability in necrotic GBM. a and **b,** Fluorescence imaging (left) and quantification (right) of TUNEL (**a**) and MDA (**b**) staining in SB28 spheroids treated for 7 days with or without 40 μM DGAT1i and 25 μM erastin (mean fold of untreated control ± s.e.m., $n \geq 8$ spheroids per condition). **c**, Live-cell imaging-based quantification of cytotoxicity (left) and GFP fluorescence (middle) in SB28 spheroids treated with or without 40 μM DGAT1i and 25 μM erastin, together with representative images (right) 120 h after treatment initiation (mean fold of untreated control ± s.e.m., $n \geq 20$ and $n = 6$ spheroids from 4 and 1 independent experiments for cytotoxicity and GFP fluorescence, respectively). **d**, Cytotoxicity rescue analyses performed as in (**c**) following treatment with 1 μM ferrostatin-1 (Fer-1) or 1 μM liproxstatin-1 (Lip-1), together with representative images (right) 48 h after treatment initiation (mean fold of untreated control ± s.e.m., $n \geq 14$ spheroids from 3 independent experiments). **e**, Schematic illustration of the experimental design for orthotopic SB28 implantation followed by continuous intracranial delivery of DGAT1i and/or erastin via osmotic pumps for 14 days. **f**, Kaplan-Meier survival curves of mice bearing orthotopic SB28 tumours treated with sham pumps (control, $n = 10$), DGAT1i (80 μM, $n = 10$), erastin (50 μM, $n = 9$), or the DGAT1i-erastin combination ($n = 11$). **g**, Schematic model illustrating how necrotic debris scavenging promotes LD-mediated lipid buffering and compensatory anti-ferroptotic adaptation, and how co-targeting these pathways creates a therapeutic vulnerability in GBM. Significance was determined by one-way ANOVA (**a**,**c**,**d**), two-sided unpaired *t*-test (**b**), or log-rank (Mantel-Cox) test (**f**). Scale bars, 50 μm (**a**,**b**) and 400 μm (**c**,**d**).

Extended data figure legends

Extended Data Fig. 1. Characterization of necrotic debris-induced lipid buffering. a, Fluorescence imaging of LDs in a GBM tumour section (N, outlined necrotic region; representative of ≥ 5 patients). **b,** Fluorescence imaging of LDs (left) and LD quantification (right) in single-cell suspension (SCS) from freshly resected matched viable and necrotic areas of a representative GBM tumour (mean fold of Viable ± s.e.m., $n \geq 3$ areas per condition). **c,** Fluorescence imaging of GLUT1 (left), TUNEL (middle) and LDs (right) in U3017MG spheroids (representative of n ≥ 5 spheroids). Outlined central hypoxic/necrotic core. **d,** Fluorescence imaging of LDs (top) and H&E staining (bottom) in an orthotopic SB28 tumour section (N, outlined necrotic region; representative of n ≥ 5 tumours). **e,** Schematic illustration of the generation of NecD, NecD-P, NecD-IR and NecD-Starv. **f,** Fluorescence imaging of LDs (left) and LD quantification (right) in U3017MG cells treated with or without 20x NecD-IR for 48 h (mean fold of untreated control (no NecD-IR) ± s.e.m., $n = 3$ areas per condition). **g,** Fluorescence imaging of LDs (U3017MG, left) and LD quantification (right) in U3017MG and U3054MG cells treated with or without 20x NecD-Starv for 48 h (mean fold of untreated control ± s.e.m., $n \geq 10$ areas per condition, analysed independently for each cell culture). **h,** Fluorescence imaging of LDs (left) and LD quantification (right) in U87MG and SB28 cells treated with the indicated NecD concentrations for 48 h (mean fold of untreated control ± s.e.m., $n \geq 20$ areas per condition, from ≥ 2 independent experiments per cell line). **i,** Fluorescence imaging of LDs (left) and LD quantification (right) in U3017MG and U3031MG cells treated with or without 20x NecD for 2 to 48 h (mean fold of 2 h ± s.e.m., $n = 3$ areas per condition, analysed independently for each cell culture). **j** and **k** Fluorescence imaging of LDs (**j**; representative images from U3017MG and U3031MG) and LD quantification (**k**) in U3013MG, U3017MG, U3031MG and U3065MG cells

1235 treated with or without 20x NecD-P pellet or the matched volume of NecD-P supernatant for 48 h
1236 (mean LD area per cell ± s.e.m., $n \geq 2$ areas per condition, analysed independently for each cell
1237 culture). **l,** Fluorescence imaging of LDs (top) and LD quantification (bottom) in U3054MG cells
1238 treated with or without 20x NecD for 24 h following 2 h pre-treatment and continuous treatment
1239 with 50 μM Fasnall or GSK219 (mean fold of NecD ± s.e.m., $n = 24$ areas per condition from 2
1240 independent experiments). Significance was determined by one-way ANOVA (**h,i,k,l**) or two-
1241 sided unpaired *t*-test (**b,f,g**). Scale bar 500 μm (**a, d** (zoomed, right)), 20 μm (**b,f,g,h,i,j,l**), 100 μm
1242 (**c**) or 1,000 μm (**d,** left).

Extended Data Fig. 2. Characterization of necrotic debris scavenging. a, Fluorescence imaging of U87MG donor cells labelled with the indicated metabolite trackers, as depicted in **Fig. 1f**. **b,** Fluorescence imaging of metabolite-labelled NecD uptake for 2 h in U3017MG and U3065MG recipient cells (representative of ≥ 3 independent experiments). **c** and **d,** Fluorescence imaging of Bodipy-DA labelled NecD-P uptake for 2 h (**c**) and co-localization with EEA1 (**d**) in U87MG. **e** and **f,** Fluorescence imaging of L-azidohomoalanine (Ala), palmitic acid (PA), or Bodipy-DA (DA) labelled NecD uptake for 2 h and co-localization with EEA1 in U87MG (**e**) and U3031MG (**f**). **g,** Flow cytometry quantification of Bodipy-DA labelled NecD uptake for 2 h in SB28 according to NecD concentration (MFI ± s.e.m., $n \geq 4$ biological replicates from 2 independent experiments; statistical comparison with 0x NecD). **h,** Flow cytometry quantification of Bodipy-DA labelled NecD-P uptake for 2 h in SB28 according to NecD-P concentration (MFI ± s.e.m., $n = 4$ biological replicates; statistical comparison with 0x NecD-P). **i,** Flow cytometry quantification of Bodipy-DA labelled NecD-IR uptake for 1 h in U3065MG according to NecD-IR concentration (MFI ± s.e.m., $n = 4$ biological replicates; statistical comparison with 1x NecD-IR). **j,** Flow cytometry quantification of 20x Bodipy-DA labelled NecD uptake in SB28 according to uptake time (MFI ± s.e.m., $n \geq 4$ from 2 independent experiments; statistical comparison with t = 0). **k,** Flow cytometry quantification of 2x Bodipy-DA labelled NecD uptake at 37 °C or 4 °C for 1 h in U87MG (mean fold 37 °C of ± s.e.m., $n = 9$ from 3 independent experiments). **l,** Flow cytometry quantification of 10x Bodipy-DA labelled NecD uptake with or without competition by 10x unlabelled NecD for 1 h in U87MG (mean fold of NecD ± s.e.m., $n = 6$ from 2 independent experiments). **m** and **n,** Flow cytometry quantification of 2x Bodipy-DA labelled NecD uptake for 1 h in U87MG with or without (CTRL) overnight pre-incubation of NecD at 56 °C or with trypsin (**m** and **n**; mean fold of CTRL ± s.e.m., $n = 3$ biological replicates). **o,** Flow cytometry

quantification of 2x Bodipy-DA labelled NecD uptake or uptake of the corresponding soluble fraction from the NecD preparation for 1 h in U87MG (mean fold of NecD ± s.e.m., n = 3 biological replicates). **p,** Flow cytometry quantification of 2x Bodipy-DA labelled NecD uptake for 1 h in U87MG following 2 h pre-treatment with or without Rac1 inhibitor (Rac1i; 100 μM, left) or 5-(N-ethyl-N-isopropyl)amiloride (EIPA) (10 μM, right) (mean fold of untreated control ± s.e.m., n = 9 from 3 independent experiments, and n = 5 from 2 independent experiments, respectively). **q,** Fluorescence imaging of Bodipy-DA labelled NecD uptake in U3017MG and U3031MG for 1 h with or without MCD (1 or 2.5 μM), or Dynasore (50 or 100 μM). **r,** Flow cytometry quantification of 2x Bodipy-DA labelled NecD uptake for 2 h in U3017MG, U3065MG, U3031MG and U3054MG (MFI ± s.e.m., n = 3 biological replicates per cell line). **s,** Flow cytometry quantification of CtxB uptake for 2 h in U3017MG, U3065MG, and U3031MG (mean fold of U3017MG ± s.e.m., n = 6 from 2 independent experiments). **t,** Fluorescence imaging (left) and quantification (right) of LD formation in U87MG and U3054MG treated with or without NecD for 24 h following 2 h pre-treatment and continuous treatment with MCD (5 μM) or Dynasore (20 μM) (mean fold of NecD ± s.e.m., $n \geq 3$ and n = 20 images per condition for U87MG and U3054MG, analysed independently for each cell line). **u**, Fluorescence imaging of LD formation and Bodipy-DA labelled NecD-P uptake after 4 h in U87MG. Significance was determined by one-way ANOVA (**g,h,i,j,r,s,t**), or two-sided unpaired t-test (**k,l,m,n,o,p**). Scale bars 10 μm (**a,b,c,d,f,q,u**), or 20 μm (**e,t**).

Extended Data Fig. 3. Characterization of NecD-induced GBM fitness. a, ssGSEA scores of the NecD transcriptional signature in patients from the TCGA-GBM (n = 287) and TCGA-LGG (n = 515) cohorts. **b**, ssGSEA scores of the NecD transcriptional signature in patients with primary (n = 231) or recurrent (n = 9) tumours from the TCGA-GBM cohort. **c**, Representative images (left) and spheroid area quantification (right) of U87MG spheroids generated from cells pretreated with or without 48 h NecD (mean fold of untreated control ± s.e.m., n = 4 spheroids). **d**, MTT assay of U3065MG treated with 20x NecD-IR for 48 h (mean fold of untreated control ± s.e.m., n = 4 biological replicates). **e**, Crystal violet quantification of cell number in U3017MG (left) and U3047MG (right) following 96 h treatment with 20x matched U3017MG- or U3047MG-derived NecD or NecD-IR (mean fold of untreated control ± s.e.m., $n \geq 6$ from 2 independent experiments). **f**, Crystal violet quantification of U3017MG cell number 72 h after 6 Gy irradiation, following 24 h pretreatment and continuous treatment with 20x NecD (mean fold of untreated control ± s.e.m., $n \geq 11$ from 3 independent experiments). **g**, Crystal violet quantification of U3031MG cell number 72 h after 2 Gy irradiation, following 24 h pretreatment and continuous treatment with the indicated NecD concentrations (mean fold of untreated control ± s.e.m., $n \geq 8$ biological replicates from 3 independent experiments). **h**, Selected enriched pathways (FDR < 0.05) identified by GSEA in U3017MG 6 h after 2 Gy irradiation, with or without 48 h NecD pretreatment. **i**, Whole-brain sections (representative of n = 5 mice per condition) collected 21 days after orthotopic implantation of U87MG cells pretreated with or without 20x NecD for 48 h. Tumours are outlined. Scale bars, 1,000 μm. Significance was determined by two-sided unpaired t-test **(a-d),** one-way ANOVA **(e,f,g),** or Benjamini-Hochberg-adjusted nominal p value (**h**).

Extended Data Fig. 4. Necrotic debris scavenging promotes inflammatory signalling and myeloid-cell lipid accumulation. a, Transcript levels of the indicated genes from transcriptomic profiling of U3017MG treated with or without 20x NecD for 48 h (log2 fold change relative to untreated control, $n = 3$ biological replicates per condition). **b**, *IL1B* expression determined by RT-qPCR in U3017MG, U3031MG and U3065MG treated with or without 20x NecD for 48 h (mean fold of untreated control ± s.e.m., $n = 3$ biological replicates with 3 technical replicates per condition). **c**, Experimental design for conditioned medium (CM) preparation (1), primary monocyte isolation (2), and CM treatment of monocytes and macrophages. **d**, Flow cytometry quantification of primary human CD14+ monocyte migration towards CM from control or NecD-preconditioned U3017MG, U3065MG and U3031MG cells (mean fold of untreated control ± s.e.m., $n \geq 11$ from 2 independent experiments using 4 independent monocyte donors for U3017MG and U3065MG CM, and $n \geq 5$ from 2 independent experiments using 2 independent monocyte donors for U3031MG CM). **e**, Fluorescence imaging (left; U3065MG CM) and quantification (right) of LD formation in macrophages cultured under hypoxia for 24 h with the indicated CM (mean fold of untreated control ± s.e.m., $n \geq 7$ areas from 1 independent monocyte donor for U3017MG CM and 2 independent monocyte donors for U3065MG CM). **f**, Flow cytometry quantification of surface PD-L1 expression in macrophages cultured under hypoxia for 24 h with the indicated CM (mean fold of untreated control ± s.e.m., $n \geq 5$ biological replicates from 2 independent macrophage donors). **g**, Fluorescence imaging of LDs and F4/80 (left) and quantification of F4/80-positive area in viable and perinecrotic regions of SB28 tumours (right; mean fold of matched viable region, $n \geq 4$ areas per tumour from 8 independent tumours). Significance was determined by two-sided unpaired *t*-test with two-stage step-up correction

(Benjamini, Krieger and Yekutieli) (**a**,**b**), one-way ANOVA (**d**,e,**f**), or two-sided unpaired *t*-test (**g**). Scale bars, 10 μm (**e**) and 100 μm (**g**).

Extended Data Fig. 5. Characterization of LD-dependent tumour fitness. a, Quantification of LDs in U3013MG, U3017MG, U3031MG and U3065MG 48 h after treatment with 20x NecD-P, with or without 40 μM DGAT1i (LD area per cell ± s.e.m., n = 3 areas per condition). **b,** Fluorescence imaging (left) and quantification (right) of LDs in U3017MG and U3065MG 48 h after treatment with or without 10x NecD-IR and 40 μM DGAT1i (mean fold of NecD-IR ± s.e.m., $n \geq 3$ areas per condition). **c,** Flow cytometry quantification of Bodipy-DA labelled NecD uptake for 2 h in U3017MG and U3065MG with or without 40μM DGAT1i (mean fold of NecD ± s.e.m., $n \geq 11$, from 4 independent experiments). **d,** Crystal violet quantification of U3017MG cell number following 48 h treatment with or without 20x NecD-IR and 40 μM DGAT1i (mean fold of untreated control ± s.e.m., n = 6, from n = 2 independent experiments). **e,** Fluorescence imaging (left) and quantification (right) of LDs in U3017MG treated with 20x NecD for 48 h (pulse), followed or not by 72 h without NecD (Chase, consumption phase), with or without 100 μM ATGL inhibitor (ATGLi; mean fold of pulse ± s.e.m., n = 60 areas per condition). **f,** Crystal violet quantification of U3017MG cell number after 96 h treatment with or without 20x NecD and 100 μM ATGLi added 24 h after NecD (mean fold of untreated control without NecD ± s.e.m., n = 22, from 4 independent experiments). **g,** Fluorescence imaging of LDs in SB28 spheroid cryosections after 48 h treatment with or without 40 μM DGAT1i. Significance was determined by two-sided unpaired *t*-test (**a,b,c,e,f**), or one-way ANOVA (**d**). Scale bars 20 μm (**b,e**) and 50 μm (**g**).

Extended Data Fig. 6. Characterization of compensatory anti-ferroptotic programs. a, *SLC7A11* expression determined by RT-qPCR in U3017MG (left) and U3065MG (right) treated with or without 20x NecD and 40 μM DGAT1i for 48 h (mean fold of untreated control ± s.e.m., n = 3 biological replicates with 3 technical replicates per condition). **b,** *SLC7A11* expression determined by RT-qPCR in U3017MG, U3031MG and U3065MG (all combined) treated with or without 20x NecD-P and 40 μM DGAT1i for 48 h (mean fold of untreated control per cell line ± s.e.m., n = 3 biological replicates with 3 technical replicates per condition). **c,** Fluorescence imaging of LDs and SLC7A11 in a representative SB28 tumour section (representative of n ≥ 10 tumours). **d,** Fluorescence imaging of LDs and SLC7A11 in a representative LGG specimen (representative of 3 tumours). **e,** Fluorescence imaging of SLC7A11 in U3065MG spheroids after 48 h treatment with or without 40 μM DGAT1i. **f**, Representative live-cell fluorescence imaging of lipid peroxidation measured using C11-BODIPY581/591 in U3065MG cells pretreated with or without NecD for 48 h followed by 6 h erastin treatment (related to **Fig. 4k**). **g,** Representative live-cell fluorescence imaging of labile Fe^{2+}, detected using FerroOrange, in U3017MG cells pretreated with or without NecD for 48 h followed by 4 h erastin treatment (related to **Fig. 4l**). Significance was determined by one-way ANOVA with Two-stage step-up (Benjamini, Krieger, and Yekutieli) (**a**), or one-way ANOVA (**b**). Scale bars 1,000 μm (**d**), 100 μm (**e**), 50 μm (**c**) and 20 μm (**f,g**).

Extended Data Fig. 7. Characterization of therapeutic vulnerabilities created by disruption of LD buffering. a, Lipid peroxidation analyses performed as in **Fig. 5a** in U3031MG, U3065MG, U3013MG and U87MG spheroids ($n \geq 10$, $n \geq 9$, $n = 5$ and $n = 15$ spheroids, from $n \geq 2$, $n = 2$, $n = 1$ and $n = 3$ independent experiments, respectively). **b,** *CPT1A* expression determined by RT-qPCR in U3017MG (left) and U3065MG (right) treated with or without 20x NecD and 40 μM DGAT1i for 48 h (mean fold of untreated control ± s.e.m., $n = 3$ biological replicates with 3 technical replicates per condition). **c,** Fluorescence imaging of LDs, SLC7A11, CPT1A, and TUNEL in a representative perinecrotic region of a human GBM tumour (representative of 3 tumours). **d**, Lipid peroxidation analyses performed as in **Fig. 5b** in U3031MG, U3065MG and U3013MG spheroids ($n \geq 10$, $n \geq 9$ and $n = 10$ spheroids, from $n \geq 2$, $n = 2$ and $n = 2$ independent experiments, respectively). **e**, Cytotoxicity analyses performed as in **Fig. 5e** in U87MG, U3013MG, U3031MG, U3047MG, U3054MG and U3065MG spheroids ($n = 10$, $n \geq 20$, $n \geq 12$, $n \geq 8$, $n \geq 23$ and $n = 20$ spheroids, from $n = 2$, $n \geq 4$, $n = 3$, $n \geq 2$, $n \geq 5$ and $n = 4$ independent experiments, respectively). **f**, Cytotoxicity analyses performed as in **Fig. 5f** in U87MG, U3013MG, U3031MG, U3054MG and U3065MG spheroids ($n = 10$, $n = 23$, $n \geq 12$, $n \geq 14$ and $n = 15$ spheroids, from $n = 2$, $n = 5$, $n \geq 3$, $n \geq 3$ and $n = 3$ independent experiments, respectively). **g**, Cytotoxicity analyses performed as in **Fig. 5e** following combined inhibition of DGAT1 and GPX4 using 10 μM RSL3 in U3017MG and U3054MG spheroids ($n \geq 8$ and $n = 10$ spheroids, from 2 independent experiments for each cell culture). **h**, Cytotoxicity analyses performed as in **Fig. 5g** in U3054MG and U3065MG spheroids treated with 40 μM DGAT1i, 25 μM erastin, and 100 μM α-tocopherol ($n = 5$ spheroids per cell culture, from 1 independent experiment). **i**, Cytotoxicity analyses performed as in **Fig. 5h** in U87MG and U3013MG spheroids treated with 40 μM DGAT1i, 100 μM etomoxir, and 100 μM α-tocopherol ($n \geq 8$ and $n = 5$ spheroids, from 2 and 1

1389 independent experiments, respectively). Significance was determined by one-way ANOVA
1390 (**a,b,d,e,f,g,h,i**) or two-sided unpaired *t*-test (**a**, U87MG; **d**, U3013MG). Scale bars 50 μm (**c**).

Extended Data Fig. 8. Characterization of therapeutic vulnerabilities created by combined targeting of LD buffering and anti-ferroptotic pathways. a and **b,** Fluorescence imaging (left), and quantification (right) of TUNEL (**a**) and MDA (**b**) staining in SB28 spheroids treated for 7 days with or without 40 μM DGAT1i and 10 μM RSL3 (mean± s.e.m., $n \geq 14$ spheroids per condition). **c**, Cytotoxicity rescue analyses performed as in **Fig. 6c** following combined inhibition of DGAT1 and GPX4 using 10 μM RSL3, with or without 1 μM ferrostatin-1 or 1 μM liproxstatin-1, together with representative images (bottom) 48 h after treatment initiation (mean fold of untreated control ± s.e.m., $n = 15$ spheroids from 3 independent experiments). **d,** Cytotoxicity and lipid peroxidation analyses performed as in **Fig. 5g** in U87MG spheroids treated with 40 μM DGAT1i, 25 μM erastin, 1 μM ferrostatin-1, and 1 μM liproxstatin-1 ($n = 15$ spheroids from 3 independent experiments). **e**, Bioluminescence imaging of mice bearing orthotopic SB28 tumours showing luciferase signal over time, normalized to non-tumour bearing mice (left) and representative images 7 days after tumour implantation (right, $n = 3$ mice). Significance was determined by one-way ANOVA (**a**,**c**,**d**) or two-sided unpaired *t*-test (**b**). Scale bars, 50 μm (**a**,**b**) and 400 μm (**c**).

Extended Data Table 1 – Affymetrix transcriptomics gene expression array, sheet 1 = NecD vs CTRL (related to Fig 2a,b), and Sheet 2 = related to Extended Data Fig. 3h, Sheet 3 = related to Fig. 4a,b,d.

Extended Data Table 2 – GSEA pathway analysis related to Fig. 2a.

Extended Data Table 3 – GSEA pathway analysis related to ED Fig. 3h.

Extended Data Table 4 – GSEA pathway analysis related to Fig. 4a,b.

Supplementary Files

This is a list of supplementary files associated with this preprint. Click to download.

- ExtendedDataTable1Sheet1p1519Sheet2p5202074Sheet3p20754091.pdf
- ExtendedDataTable2.pdf
- ExtendedDataTable3.pdf
- ExtendedDataTable4.pdf
- TalbotetalExtendedDataFigures18.pdf